Growth and characterization of highly stable and layered 2D/3D perovskites for solar cells

by

Sandile Job Thubane

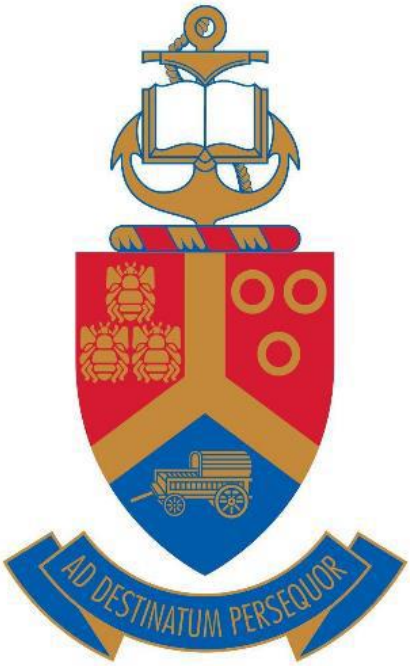

Submitted in partial fulfillment of the requirements for the degree

Magister Scientiae
In the Faculty of Natural and Agricultural Science
Department of Physics

Supervisor: Prof. M. M. Diale

Co-supervisor: Dr. N. Nombona

February 2022

DECLARATION

I, Sandile Job Thubane, declare that the dissertation, I hereby submit for the degree Magister Scientiae (MSc) in the department of Physics at the University of Pretoria is my work and has not been submitted previously by me for a degree at this or any other institution.

Signature 

Date 18/02/2022

DEDICATION

To my late mother Letty Thubane

&

To my siblings Dumisane Lucas Thubane, Markos Thubane, Zakhele Rahlogo, and Lettie Rahlogo

ACKNOWLEDGMENTS

- My deepest gratitude goes to my supervisor, Prof. M. Diale, for the opportunity to work under her guidance and for her support, and dedication towards the completion of this study.
- I would like also like to thank Prof. Theron for giving me the opportunity to be a part of the physics department.
- I would like to thank the University of Pretoria for providing me with the opportunity to further my studies.
- My thanks also goes out to all the members of Green and Clean Energy group for all their encouragement
- Thank you Dr. Fru and Dr. Justine for proofreading my chapters before submission and for helping me compile this dissertation.
- Our collaborators in the Department of Chemistry at the University of Pretoria contributed the XRD measurements. Sincerest thanks to all the workers in the Laboratory for Microscopy and Microanalysis.
- Thank you Dr. Nombona for providing me office space in their Department
- I would like to also thank Prof. David Cahen for allowing me to come to his lab
- Thank you to the Weizmann Institute of Science and Bar-Ilan University for providing me with the enabling environment for my experiments.
- I would like to express my gratitude to the Nanotechnology group for giving me the space to also work in their laboratory
- My deepest gratitude goes to my late mother for her unwavering support and encouragement

Abstract

Perovskites of cesium lead halide ($CsPbX_3$, X = Cl, Br, I) have received a lot of attention due to their relative stability in comparison to their organic-inorganic counterparts. This study synthesized a thin film of cesium lead tribromide ($CsPbBr_3$) by spin coating followed by dip coating and characterized it through a scanning electron microscope (SEM), ultraviolet-visible (UV- Vis) spectrometer, and X-ray diffraction (XRD) in order to observe its morphological, optical and structural characteristics. SEM micrographs revealed pinholes within the perovskite film that significantly impacted device performance. To address this issue, we show that spin-coating phenethylammonium bromide (PEABr) on $CsPbBr_3$ thin films improves morphology and surface coverage. The optical study of $CsPbBr_3$ thin film showed a broad UV-Vis absorption with an onset at 530 nm and an excitonic peak at 515 nm. However, $CsPbBr_3$/PEABr preserves the optical properties of $CsPbBr_3$. Additionally, two excitonic peaks appear at 405 and 436 nm which are attributed to a 2D perovskite $PEA_2Cs_{n-1}Pb_nBr_{3n+1}$ with n = 1 and n = 2 phase. The viscosity of PEABr was also suggested to play a role in the decrease followed by an increase in absorption of $CsPbBr_3$/PEABr films. XRD results of $CsPbBr_3$ film showed the impurity phase of $CsPb_2Br_5$ and a cubic $CsPbBr_3$ structure with the *Pm-3m* space group. Furthermore, PEABr had no effect on the intrinsic crystal structure of $CsPbBr_3$. The $CsPbBr_3$ solar cell produced a low open-circuit voltage (V_{oc}) of 0.3 eV and a fill factor (FF) of 30.89%, which may due to the loss of charge-carriers in the area with pinholes. This could also explain the device's low power conversion efficiency (PCE) of 0.9%. A mixed-cation solar cell based on $CsMAFAPb(IBr)_3$ was also designed and fabricated. This solar cell showed a photoluminescence emission at 766 nm with a charge carrier lifetime of 24 ns, which indicates that it is less prone to degradation. Current density-voltage (J-V) characteristics of $CsMAFAPb(IBr)_3$ show a V_{oc} and a FF of 1.14 eV and 57.32%, respectively. With this device, PCE of 13.89% was also achieved, with a short-circuit current of 23 $mA/cm^{2.}$ We conclude that these results may be related to the low hysteresis experienced at low voltage scan speeds of 10 mV/s. All things considered, the addition of an organic spacer to a 3D perovskite improves the morphological, optical, and structural characteristics of the as-prepared 3D perovskite film.

Table of content

List of figures

List of tables

Chapter 1

1 Introduction

1.1 Global energy demand

Energy is key to any country's economic development and prosperity. It is linked to the world's most pressing issues such as global environmental change, poverty alleviation, and food security [1]. One of the pressing challenges of the 21st century is the growing energy crisis [2]. The demand for energy rises directly in proportion to a country's population and economic growth. According to the International energy outlook (2021), total world energy demand is expected to increase by 47% between 2020 and 2050 [3] as shown in *Figure 1-1*. The energy demand should match the energy supply from renewable energy resources such as wind, solar, biomass and biofuels, and geothermal as they are abundant. Nevertheless, nearly 85% of the world's energy is produced by non-renewable sources of energy [4]. These non-renewable energy sources such as fossil fuels (oil, coal, natural gas, and nuclear energy) are depleting [5] and thus giving rise to the need for renewable energy sources. Over the period 2020 to 2050, renewable energy demand is expected to increase from 15% to 27%.

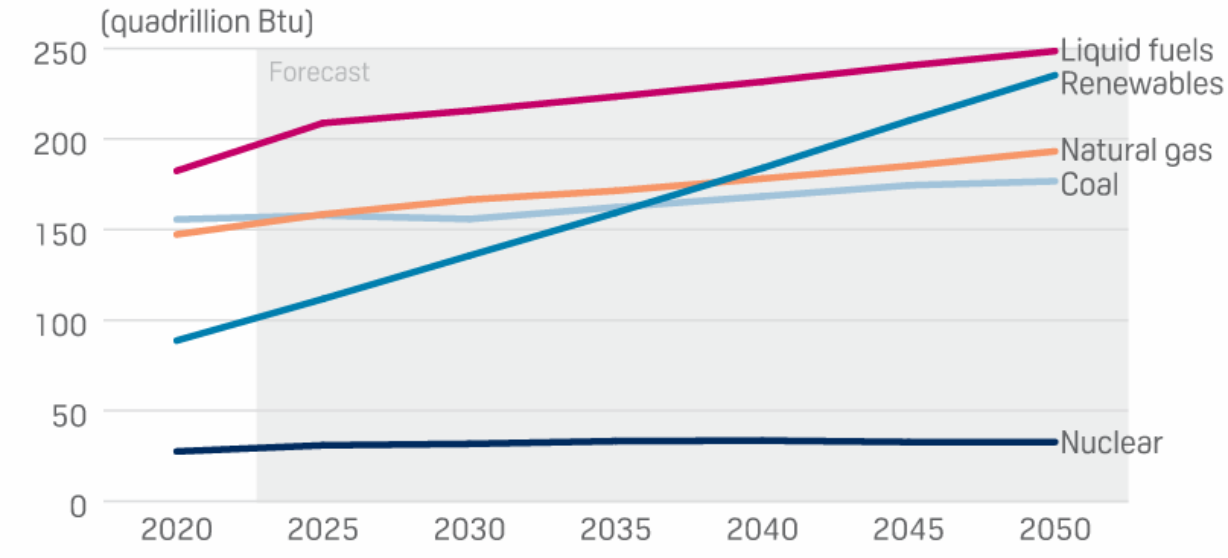

Figure 1-1: Demand for energy from 2020 to 2050 [5].

The current global energy scenario, which is dominated by fossil fuels, has concerns about regional climates (how windy, rainy, and what temperatures are like for different regions), environmental degradation, fuel resource depletion, and energy security. Furthermore, nuclear power facilities have severe drawbacks, such as their nuclear waste which have a negative impact on the environment. The use of renewable energy sources is therefore crucial to the global development of a sustainable electric power system. *Figure 1-2* shows the percentage of energy generated from different energy sources. The sun is the planet's most abundant energy source. Solar energy falls at a rate of 1 kW/m^2 on the earth's surface, which indicates that the amount of energy received from the sun in a single day may meet the entire world's energy requirement for more than 20 years [6]. However, it is one of the least energy sources used (3.2%) to generate electricity. This may be due to the availability of expensive and inefficient solar devices.

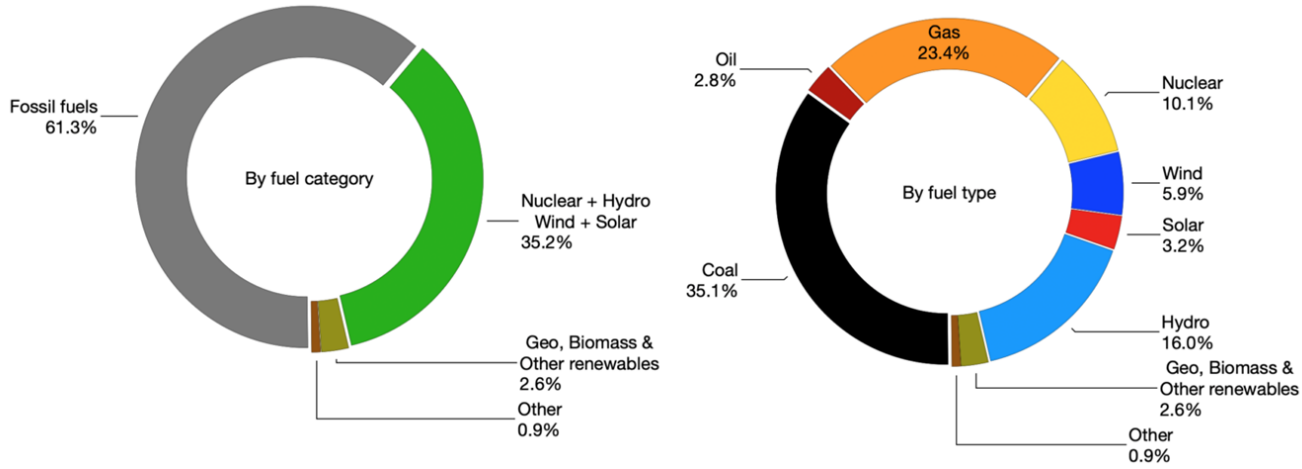

Figure 1-2: The world’s energy generation charts [4].

The development of an inexpensive, limitless, and clean solar power technical innovation has enormous long-term benefits since it improves the country’s power security by providing an import-independent source, resulting in enhanced durability, decrease environmental dangers, and lower costs [2, 7]. The potential of solar energy is beneficial in many ways. The majority of fossil fuels, for example, contribute to climate change and, subsequently, socioeconomic degradation caused by poor environmental quality; other options include leveraging solar energy for electrical needs from tropical and sub-tropical regions because they

receive more solar radiation throughout the year. In addition to being more sustainable than fossil fuels, solar energy is also environmentally beneficial, and its usage has become more widely accepted because of its reliability and efficiency [8]. Solar power systems can be used in both urban and rural settings.

1.2 Operation and applications of solar cells.

The use of a stable, non-toxic, abundant, and well-understood photoactive absorber material makes silicon solar cells advantageous. With an energy band gap of 1.12 eV, silicon has an approximate cutoff wavelength for light absorption of 1160 nm. This band gap is very close to the ideal value for solar energy conversion using a single semiconductor optical absorber, and it is well suited to the solar spectrum. The theoretical conversion efficiency limit for a semi-infinitely thick silicon solar cell is 33.5% at 25 °C when only radiative recombination is taken into account [14] . Modern photovoltaic cells have an energy efficiency of 15 to 20%, which implies that huge and expensive assemblies of such cells are required to generate moderate amounts of power [10]. This type of cell is shown in *Figure 1-3*.

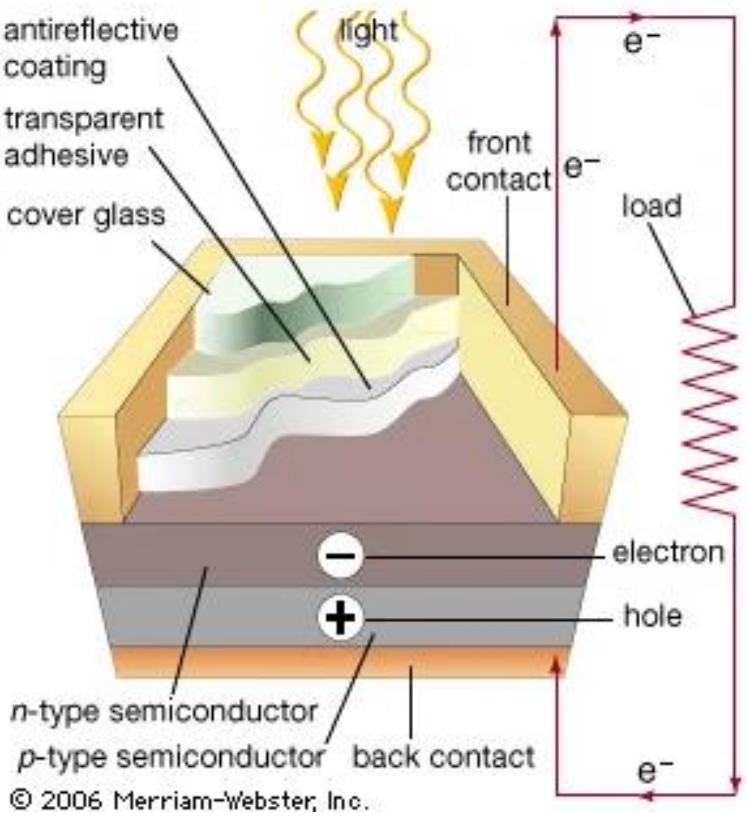

Figure 1-3: Architecture of a basic solar cell [10].

One of the most promising markets for renewable energy is the use of photovoltaic panels to harness solar radiation and generate electricity. The photovoltaic market is increasingly more hotly contested globally because of its potential for rapid expansion and high levels of investment. Based on the type of light-absorbing substance in the photoactive layer, solar cells can be readily divided into different types (Table 1). Devices made of crystalline silicon rely on a p-n junction to separate charges and enable effective production of photocurrent and photovoltage. This junction is created by spatially guided doping of a planar silicon (Si) structure.

Figure 1-4: Solar-power plant with a concentrated array [10].

Many nations use solar energy to evaporate seawater and make salt, for example. Similarly, solar-powered desalination systems convert salt water into drinkable water by converting solar energy into heat, which is then used to accelerate the desalination process, either directly or indirectly. Additionally, solar technology has emerged as a clean and renewable way to produce hydrogen. A solar-powered artificial leaf, which mimics photosynthesis, uses solar energy to split water into hydrogen and oxygen, leaving very little contamination behind. More effort will be required to increase the efficiency and cost-effectiveness of these devices for industrial use.

1.3 Evolution of solar cell materials

The solar cells' architecture limits electron transport to one direction, allowing them to be collected for useful electricity. The NREL (National Renewable Energy Laboratory) of the United States has reviewed the improvement in cell efficiency with technological advancement as shown in *Figure 1-5* [11]. The first-generation solar cells, depicted in blue in *Figure 1-5*, are made of crystalline silicon materials that can absorb sunlight and have consistent cell efficiencies. The second-generation thin film was developed in response to the high material usage and cost of silicon solar cells. The maximum film thickness for this generation was reduced to a few nanometers to tens of micrometers in order to save material utilization. Meanwhile, many researchers have utilized light management concepts in dye-sensitized solar cells (DSSCs), perovskite, organic solar cells, photochemical cells, QDs, nanostructuring, and nanopatterning. In the future, emerging photovoltaics, composed of dye-sensitized, polymer, and perovskite solar cells, such as the ones in *Figure 1-5*, will be substantially less expensive than traditional cells.

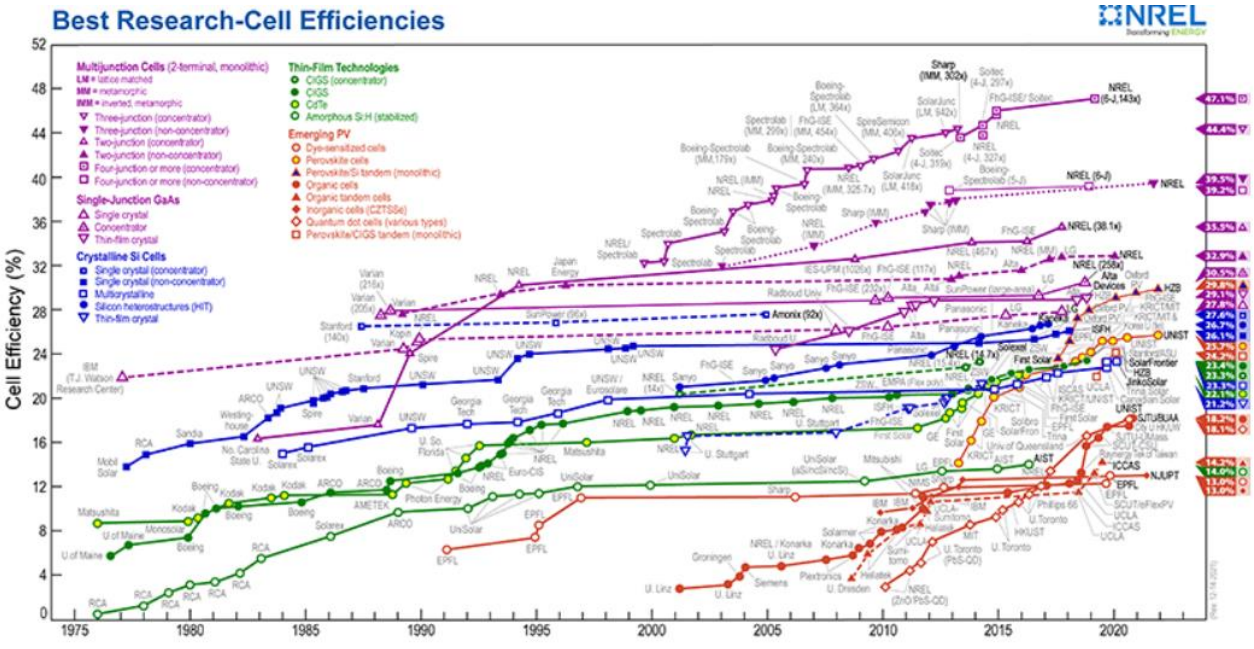

Figure 1-5: Improvement in cell efficiency in photovoltaic efficiency [11].

The four processes – light absorption, charge transfer and separation of opposite charges, charge transport, and charge collection – all need to be adjusted further to improve cell efficiency [12]. In *Figure 1-5*, the state-of-the-art conversion efficiency of perovskite tandem

solar cells is 29.8%. In comparison to silicon solar cells, perovskite solar cells are of low cost, easy to synthesise, flexible, and lightweight.

1.4 Problems in perovskite materials

In recent years, perovskites have shown a significant increase in potential by acting as light harvesters in solar cells. They have a direct bandgap, significant absorption coefficients [13], and long diffusion lengths are among their advantages [13, 14]. However, despite the significant progress in laboratory power conversion efficiency (PCE) of halide perovskite (HaP) solar cells, more work must be done before large-scale manufacturing in the industry [15, 16]. Some of these problems include poor long-term stability of the perovskite thin film and device affected by storage conditions and during operation[17, 18], environmental and operational stability of perovskite thin film and devices, solvent engineering and toxicity of lead (Pb) [16, 19], light-induced phase segregation in large bandgap mixed halide perovskites[20, 21], poor device reproducibility [19], scalable manufacturing of large-area perovskite solar cells [14, 18].

Synthesis and deposition conditions play a significant role in the stability and efficiency of fabricated solar cells. Synthesis and deposition processes of large area thin perovskite film include spay coating, doctor blade coating, screen printing [22], slot-die coating, gravure printing, ink-jet, and printing vacuum/vapour assisted deposition [23, 24]. Solvents are commonly used in solution deposition methods that are toxic, skin penetrating, and carcinogenic [20]. To move from laboratory-scale to industrial-scale, the development of greener deposition techniques, such as solution methods employing less toxic solvents [16] and accurate vacuum methods [19, 25] is necessary. To date, most of the solution processing methods of HaP solar cells may produce highly efficient devices. However, these devices suffer from instability.

For this reason, several ways to reduce or delay device degradation have been investigated [26, 27]. These include customizing 3D perovskite materials through composition engineering or the addition of additives such as ionic liquids, reducing infiltration of water into the active layer through device encapsulation with moisture-resistant layers, or using alternative device architectures with more robust HTM and/or ETM layers are some of these solutions.

1.5 Aim and objectives

This dissertation aims to develop the growth of 2D HaP from as-prepared 3D HaP thin films by solution deposition methods.

The objective are:

- To fabricate a multi-cation/anion [$CsMAFAPb(Ibr)_3$] perovskite solar cell
- To synthesize a $CsPbBr_3$ (3D) and $CsPbBr_3$/PEABr (quasi-2D) perovskite thin films
- To fabricate and characterize $CsPbBr_3$ –based solar cells

1.6 Structure of dissertation

This dissertation is divided into 5 (Five) chapters as follows:

Chapter 1 presents the background and motivation of the research work, aim and objectives as well as the structure of the dissertation.
Chapter 2 reports on literature review of organic-inorganic solar cells and thin films of different dimensions, their synthesis methods, and applications.
Chapter 3 introduces the experimental techniques used in this study as well as their characterizations.
Chapter 4 discusses the results obtained from the synthesis and characterizations of $CsPbBr_3$ and $CsPbBr_3$/PEABr thin films. A solar cell current density-voltage measurements of $CsPbBr_3$ and $CsMAFAPb(IBr)_3$ solar cells are also discussed in this chapter.
Chapter 5 discusses an overview conclusion of this study and recommends possible future work.

1.7 References

1. Purohit, I., P. Purohit, and S. Shekhar, *Evaluating the potential of concentrating solar power generation in Northwestern India.* Energy policy, 2013. **62**: p. 157-175.
2. Devabhaktuni, V., et al., *Solar energy: Trends and enabling technologies.* Renewable and Sustainable Energy Reviews, 2013. **19**: p. 555-564.
3. Outlook, A.E., *Energy information administration.* Department of Energy, 2010. **92010**(9): p. 1-15.
4. DATA, W.E. *2022*. **World Electricity Generation**; Available from: https://www.worldenergydata.org/world-electricity-generation/.
5. **Physics, L.B.** ***CASE STUDY: WORLD ENERGY USE***. **2016**; Available from: https://courses.lumenlearning.com/boundless-physics/chapter/case-study-world-energy-use/.
6. Sarbu, I. and C. Sebarchievici, *Solar heating and cooling systems: Fundamentals, experiments and applications*. 2016: Academic Press.
7. Khan, J. and M.H. Arsalan, *Solar power technologies for sustainable electricity generation–A review.* Renewable and Sustainable Energy Reviews, 2016. **55**: p. 414-425.
8. Fong, K., C.K. Lee, and T.T. Chow, *Comparative study of solar cooling systems with building-integrated solar collectors for use in sub-tropical regions like Hong Kong.* Applied energy, 2012. **90**(1): p. 189-195.
9. Arshad, R., et al. *Improvement in solar panel efficiency using solar concentration by simple mirrors and by cooling*. in *2014 international conference on robotics and emerging allied technologies in engineering (iCREATE)*. 2014. IEEE.
10. Britannica, E. *Concentrated Solar-Power plant*. [cited 2022 14 February]; Available from: https://www.britannica.com/science/solar-energy/Electricity-generation#/media/1/552905/190480.
11. Report, N. *"Photovoltaic Cell Conversion Efficiency"*. Available from: https://www.nrel.gov/pv/cell-efficiency.html.
12. Janssen, R., *Introduction to polymer solar cells.* Departments of Chemical Engineering & Chemistry and Applied Physics, Eindhoven University of Technology, The Netherlands, 2005.
13. Ball, J.M., et al., *Low-temperature processed meso-superstructured to thin-film perovskite solar cells.* Energy & Environmental Science, 2013. **6**(6): p. 1739-1743.

14. Xiao, Z., et al., *Efficient, high yield perovskite photovoltaic devices grown by interdiffusion of solution-processed precursor stacking layers.* Energy & Environmental Science, 2014. **7**(8): p. 2619-2623.
15. Caliò, L., et al., *Cu (ii) and Zn (ii) based phthalocyanines as hole selective layers for perovskite solar cells.* Sustainable Energy & Fuels, 2017. **1**(10): p. 2071-2077.
16. Kim, D.H., et al., *Outlook and challenges of perovskite solar cells toward terawatt-scale photovoltaic module technology.* Joule, 2018. **2**(8): p. 1437-1451.
17. Zhang, X., *Strain control for halide perovskites.* Matter, 2020. **2**(2): p. 294-296.
18. Fu, Q., et al., *Recent progress on the long-term stability of perovskite solar cells.* Advanced Science, 2018. **5**(5): p. 1700387.
19. Swartwout, R., M.T. Hoerantner, and V. Bulović, *Scalable deposition methods for large-area production of perovskite thin films.* Energy & Environmental Materials, 2019. **2**(2): p. 119-145.
20. Unger, E., et al., *Roadmap and roadblocks for the band gap tunability of metal halide perovskites.* Journal of Materials Chemistry A, 2017. **5**(23): p. 11401-11409.
21. Bush, K.A., et al., *Compositional engineering for efficient wide band gap perovskites with improved stability to photoinduced phase segregation.* ACS Energy Letters, 2018. **3**(2): p. 428-435.
22. Kamino, B.A., et al., *Low-temperature screen-printed metallization for the scale-up of two-terminal perovskite–silicon tandems.* ACS Applied Energy Materials, 2019. **2**(5): p. 3815-3821.
23. Liu, C., Y.-B. Cheng, and Z. Ge, *Understanding of perovskite crystal growth and film formation in scalable deposition processes.* Chemical Society Reviews, 2020. **49**(6): p. 1653-1687.
24. Kim, Y.Y., et al., *Gravure-printed flexible perovskite solar cells: toward roll-to-roll manufacturing.* Advanced science, 2019. **6**(7): p. 1802094.
25. Fru, J.N., N. Nombona, and M. Diale, *Characterization of sequential physical vapor deposited methylammonium lead tri-iodide perovskite thin films.* Vacuum, 2020. **182**: p. 109727.
26. Berhe, T.A., et al., *Organometal halide perovskite solar cells: degradation and stability.* Energy & Environmental Science, 2016. **9**(2): p. 323-356.
27. You, J., et al., *Improved air stability of perovskite solar cells via solution-processed metal oxide transport layers.* Nature nanotechnology, 2016. **11**(1): p. 75-81

Chapter 2

2 Two-dimensional halide perovskites

2.1 Introduction

The purpose of this chapter is to provide an overview of halide perovskites (HaP). The different types of methods that can be used to synthesize different types of 2D HaP are also discussed in this chapter, including their use as absorbing layers and as dopants in solar cells. Additionally, this chapter discusses the application of 2D HaP to light-emitting diodes. The degradation of 2D HaP materials is explained as well as the charge transport. This chapter also discusses the environmental effects of lead, which led to the development of lead-free 2D HaP.

2.2 Halide perovskites (HaP)

3D perovskites solar cells (PSC) have recorded an efficiency exceeding 25% [1] and are easy to synthesize at a low cost, but they have three drawbacks: instability, toxic lead (Pb), and poor reproducibility. To overcome these challenges, some research groups have focused on dimensional tailoring to stabilize the 3D [2], others have replaced the toxic Pb with tin (Sn) [3], whilst others have optimized existing methods of synthesising the perovskites materials [4]. 3D HaP have the general formula ABX_3 (*Figure 2-1*) where A is an organic cation (MA= methylammonium, FA= formamidinium or Cs^+= cesium), B is a positively charged/inorganic cation (Pb^{2+} = lead or Sn^{2+} = tin) and X is a negatively charged anion (I^- = iodide, Br^- = bromide or Cl^- = chloride), and they can assimilate into any crystal structure. This is determined by the corner-sharing BX_6 octahedra and the size of the A cation [5]. 3D HaP becomes unstable due to their hydrolysis during moisture exposure. This is caused by a reaction between A cations and water molecules [6].

Organo lead halide perovskite is an exciting material being studied for photovoltaic solar cells. The power conversion efficiency of perovskite-based solar cells has significantly improved during the last five years, surpassing energy conversion efficiencies other absorber materials. One of the primary causes of the high solar cell efficiency in organo metal halide perovskite is the recent observation of a long diffusion length of electrons and holes.

2.2.1 3D Halide perovskite tailoring

Recently, lower-dimensional HaP – particularly 2D HaP, are receiving a lot of attention thanks to their photo and chemical stability, photo-physical tunability, photo-absorption, and emission properties. Among the applications for 2D HaP are photodetectors, lasers, electroluminescent devices, solar cells, and spintronics [7-10]. Solar cells made up of 2D HaP have been shown to have a power conversion efficiency of over 15% and long-term stability of over 1 year [11, 12]. Thus, 2D HaP have emerged as more stable materials than 3D HaP, however, the problem lies in synthesising a 2D HaP without compromising the PCE when used in photovoltaics.

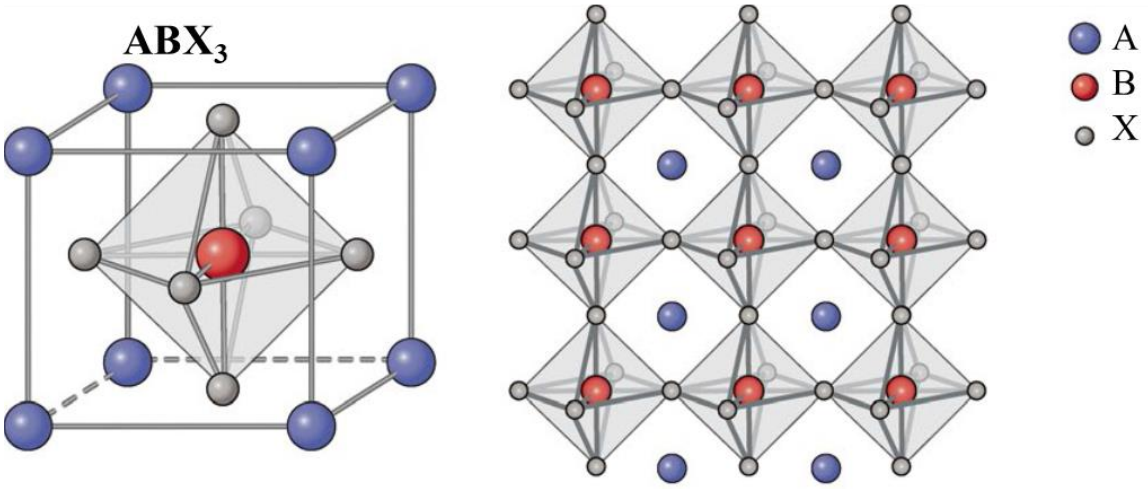

Figure 2-1: Illustration of a 3D HaP structure ABX_3 showing the corner-sharing $[BX6]^{4-}$ octahedra [13].

Dimensional tailoring of the 3D HaP results in a 2D HaP with the general formula: $R_2A_{n-1}B_nX_{3n+1}$, where R is an additional bulky organic cation (such as PEA^+ = phenethyl Ammonium, BA^+ = benzyl Ammonium, CAI = cyclopropylammonium Iodide, IEA = iodoethyl ammonium, AVA = ammonium valeric acid). The R cation acts as an organic spacer between the organic sheets (*Figure 2-2*), and *n* determines the number of inorganic layers. $[BX_6]^{4-}$ is a corner-sharing metal halide sandwiched between the inorganic barrier planes of R [13], held together by coulombic forces. Consequently, a 2D HaP can be regarded as a dependable, light-absorbing material that is moisture-resistant and photostable. The addition of a bulky organic cation (aliphatic or aromatic alkyl ammonium) partially substitutes the A cation, and it is considered the part of the HaP that is more resistant to moisture. 2D HaP have also been shown to have improved stability due to its hydrophobic nature, highly oriented structure, and dense

packing of the R ion inside the crystal; this is attributed to the flexible 2D crystal structures that present more relaxed limits to the size of organic ions. According to Du and Mitzi, the increase in the number of layers (n >1) results in a decrease in the bandgap and the exciton binding energy [13, 14]. This results in interesting optoelectronic behavior such as strong optical nonlinearity and high electroluminescence. The higher value of n ($n = \infty$), as well as the introduction of a small cation, can result in the formation of multi-layered quasi-2D HaP which will adapt to form a 3D structure. Pure 2D HaP contain a photoactive π-conjugated cation, which influences the optoelectronic behavior of the compound. As an example, when n = 1, a pure 2D HaP (R_2BX_4) is obtained as a result of the isolation of just one layer of the inorganic framework by the bulky organic cations.

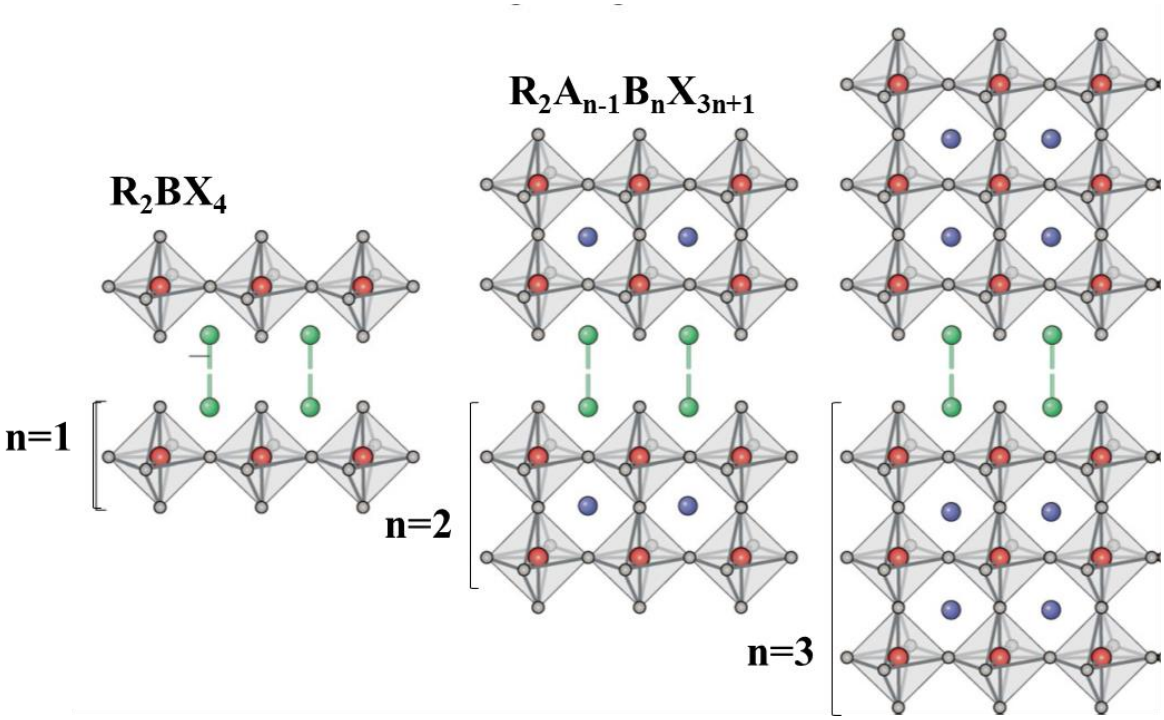

Figure 2-2: Illustration of a lower dimension HaP with different number of perovskite layers (n) [15].

HaP can be pure 2D, pure 3D, 2D/3D, or 3D/2D based on their architecture. To synthesize both the 2D/3D and 3D/2D HaP solar cell, a 2D and a 3D HaP are combined to achieve a quasi-2D hybrid HaP, which can enhance the energy alignment at the interface for charge transport and collection [16], as well as improving moisture stability [17]. A 2D HaP is hydrophobic, so when it is combined with a 3D HaP it prevents water from having direct contact with it, thus reducing grain boundaries. Gan *et al*. used a one-step spin-coating method under ambient conditions to synthesize homogeneous and pinhole-free 2D HaP films of the

formula: $(PEA)_2(MA)_{n-1}Pb_nI_{3n+1}$. The series of layers ($n$ = 1, 2, 3) exhibited high stability in 60% moisture content for over 60 days during and after experimentation while remaining unchanged. Moreover, TiO_2 nanorods were also used to improve film features, contacts, and coverage. This was done to optimize and improve the $(PEA)_2(MA)_2Pb_3I_{10}$-based devices, shown in *Figure 2-3*. The PCE of 3.72% was achieved when n = 3 and with 600 nm TiO_2 nanorods, 70% of the initial PCE was retained after 60 days of storage at 60% humidity in the dark [18].

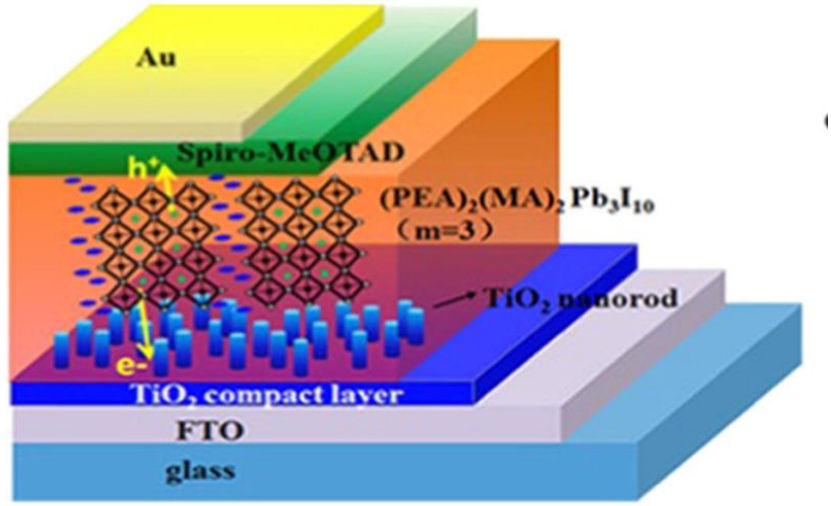

Figure 2-3: $(PEA)_2(MA)_2Pb_3I_{10}$-based device[18].

2.3 Development of 2D HaP

2.3.1 Preparation methods

Various methods have been used to synthesise 2D HaP. These methods include vapor-assisted interface optimization method which facilitates the evaporation of the organic components [19], solution processing which is a beneficial method that can provide a roll-to-roll printing for large-scale production [4], a fast-synthetic method which is very important in closing the water-air interface producing uniform orientation and fast in-plane growth [20], mechanical exfoliation or chemical vapour/atomic layer deposition which produces a clear pure-blue color emission and an increased radiative rate [21]. Recently, Chen *et al*. demonstrated that a reaction between a 3D HaP with 1,4-butanediamine iodide ($BEAI_2$) vapor can produce a HaP solar cell that is both stable and highly efficient. This was achieved by using the vapor-assisted interface optimization method on a 3D $MAPbI_3$ HaP as shown in *Figure 2-4*.

2.3.1.1 Vapor assisted and solvothermal method

The crystallization of the HaP film was induced by the incorporation of $BEAI_2$ to produce large grains (~500nm). They found that the resulting HaP solar cell produced a high PCE of 19.58% without hysteresis. Moreover, 90% of its original PCE was retained when stored under ambient atmospheric conditions, and its stability under 85 °C was better. By far, this method has produced the highest efficiency for 2D HaP using the vapor-assisted methods. Duo *et al.* reported on the atomically thin 2D organic-inorganic hybrid HaP $[(C_4H_9NH_3)_2PbBr_4]$ using a solution-phase growth method of single-and-few-unit-cell-thick single-crystalline $[(C_4H_9NH_3)_2PbBr_4]$ HaP with well-defined square shape and large size. They found that these hybrid perovskite sheets exhibit a structural relaxation that results in a shifted bandgap as compared to the bulk crystal. Furthermore, the 2D crystals exhibit efficient photoluminescence and color tuning that can be achieved by changing the sheet thickness and composition [22].

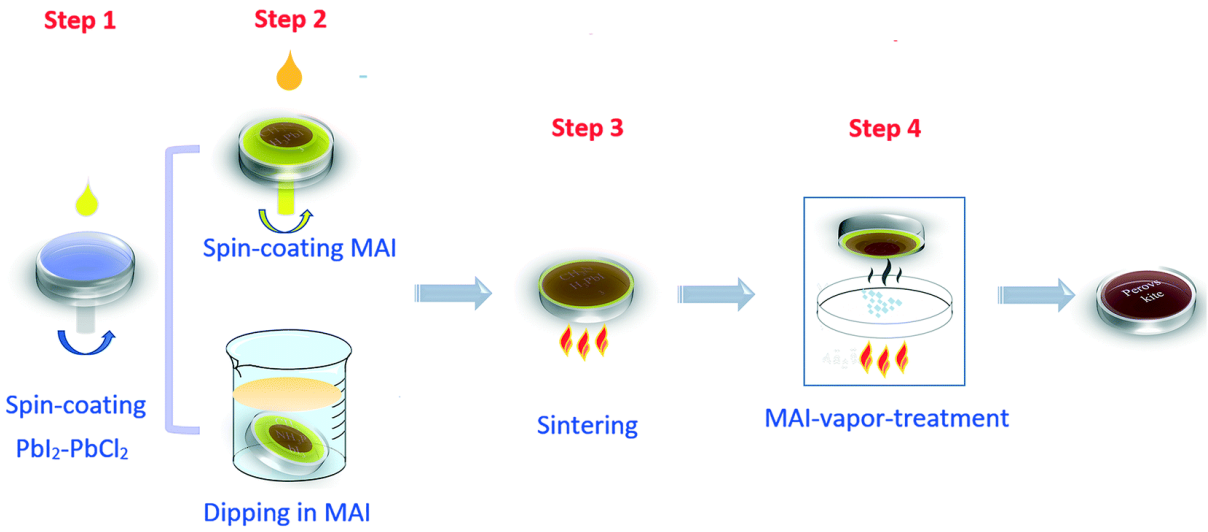

Figure 2-4: Vapour-assisted interface optimization method [23].

Rong *et al*. synthesised a single lead chloride HaP $[H_2\,(dmen)]PbCl_4$ using one-step solvothermal synthesis and they found that this compound exhibits a typical semi-conductive behaviour, with increasing conductivity as the temperature increases [24]. *Ma C et al*. solved the problem of instability in 3D HaP by substituting small organic cations such as propane-1,3-diammonium (PDA) between inorganic layers. Using electrochemical impedance spectroscopy, time-resolved photoluminescence (TRPL), and mobility measurements, they demonstrated charge confinement was enhanced due to the diminished influence of quantum confinement in PDA-based 2D HaP. The PCE of the interlayer-engineered 2D HaP yielded

13.0%. Furthermore, it was found that the 2D HaP solar cell can retain 90% of its efficiency for more than 1000 hours with encapsulation and 70% without encapsulation for more than 100 hours [25]. Whilst Koh *et al*. used a sequential deposition method under ambient conditions to produce a low-dimensional HaP containing iodoethylammonium cation $(IC_2H_4NH_3)_2MA_{n-1}Pb_nI_{3n+1}$. By varying the dipping duration, the dimensionality of this HaP could be controlled. According to their findings, when increasing the dipping duration, *n* increases, which ultimately reduces the bandgap of the material and results in a wider absorption and higher photocurrent. At dipping times of 4 min, the highest PCE was found to be 9%, and a quasi-2D HaP was seen to form at this dipping time [26]. A comparison of the performance of a fresh HaP device with a 4-day-old device that has been exposed to ambient conditions at 25 ℃ and 70-80% relative humidity unencapsulated shows the quasi-2D HaP to be stable over long periods, as mentioned by Fang *et al.* [27].

Yang *et al*. added bulky ammonium in $MAPbI_3$ to improve the properties such as the structure, electronic, and optical properties of the HaP. They used a mortar-and-pestle grinding method to acquire the mixed-cation materials. During this process, it was observed that the powder mixture changed from yellow to dark yellow, then to brown, and finally to black color with shining facets, which is characteristic of HaP. Three different bulky ammonium groups were used, that is, AMA, BAMA, and PEAMA. They found that bulky cations were not involved in the phase of $MAPbI_3$, yet these bulky cations played a crucial role in the photoluminescence properties of the material, while nanoparticles with approximated sizes of the order of tens of nanometres were observed in the scanning electron microscopy (SEM) images. They also used the Scherer equation to calculate the average crystallite sizes for AMA, BAMA, and PEAMA, which were estimated at 16.0 nm, 13.9 nm, and 8.1 nm, respectively, which was consistent with the SEM results. The difference in the crystallite sizes of the HaP material indicates that they are highly dependent on rates of reactions between the aromatic ammonium and $MAPbI_3$. Furthermore, it was concluded that the bulky ammonium cations with a stronger steric hindrance (A > BA > PEA) results in larger crystallite sizes because of the slower reaction rates but as the distance between the bulky phenyl ring and ammonium decreases (A < BA < PEA) the grain sizes are also reduced. The bandgaps of AMA, BAMA, and PEAMA were found to be 1.58 eV, 1.59 eV, and 1.61 eV, respectively, which are much larger than the bandgap for $MAPbI_3$ (1.51~1.52 eV), this suggested an influence of the organic cations on the material's bandgap although these cations do not enter the interior lattice of $MAPbI_3$ HaP. The bandgap was found to also increase with an increase in the distance between

the phenyl and the ammonium groups (A < BA < PEA). They also noticed that Anilinium distorts the resulting structure remarkably while creating defect states that extinguish the luminescence. The TRPL results have shown a longer lifetime for bulky components and a shorter lifetime for surface trap states components, these are the decay dynamics observed when using pure MA HaP [28]. The lifetime may show the competition between radiative and nonradiative pathways in the material. Comparing the three bulky cations, it was found that the longer the lifetime (BAMA > PEAMA > AMA), the material will have lesser nonradiative recombination sites [29].

2.3.1.2 Stability and power conversion efficiency of lower dimensional halide perovskites

To enhance the stability of the solar cells, researchers are using different methods of incorporating the 2D HaP into the cell as shown in *Figure 2-5*, but this decreases the PCE of the solar cell. To address the issue of reduced PCE, Yao's group developed a two-step method for producing compact 2D/3D HaP films by spin-coating a mixture of PbI_2 and polyethyleneimine hydroidide (PEI.HI) and then applying a coating layer of MAI. They found that the PbI_2 formed $MAPbI_2$ with the MAI, whereas excess PbI_2 formed a 2D HaP layer of $(PEI)_2PbI_2$ with the PEI.HI, this was accomplished by using a mole ratio of *n* ranging from 0 to 4% to achieve $(MAPbI_3)_{1-n}[(PEI)_2PbI_4]_n$. The highest PCE (16%) was observed at n = 2% with better stability than $MAPbI_3$. Under ambient conditions (RH: 50%), $MAPbI_3$ devices cease to function after 120 hours. In the mole ratio of 4%, the PCE of $(MAPbI_3)_{1-n}[(PEI)_2PbI_4]_n$ was observed to be 8%, indicating a decrease in contact between water and the HaP improves stability [30]. Ma C *et al*. used a two-step synthesis for forming $MAPbI_nCl_{3-n}/CA_2PbI_4$ [2]. This was achieved by spin coating a 3D HaP $MAPbI_nCl_{3-n}$ layer, then treating this layer with CAI, which reacts with the excess PbI_2 that is in the 3D layer to induce the formation of a 2D CA_2PbI_4 HaP layer. The 2D/3D HaP solar cell produced a PCE of 13% which was stable for 40 days without encapsulation at a relative humidity of 63 ± 5% and it was superior to a 3D solar cell under the same conditions. Yao *et al.* fabricated another 2D/3D HaP on a flexible substrate by a two-step deposition method with PEI.HI, and achieve a PCE of 13.8%. This 2D/3D bilayer was composed of $MAPbI_3$ and PEI_2PbI_4 [31]. In a similar method, Chen *et al*. used AVA^+ ($HOOC(CH_2)_4NH^{3+}$) to synthesize an ultrathin 2D HaP [AVA_2PbI_4] which was deposited on $(FAPbI_3)_{0.88}(CsPbBr_3)_{0.12}$. The resulting $(FAPbI_3)_{0.88}(CsPbBr_3)_{0.12}/AVA_2PbI_4$ hybrid HaP showed higher moisture stability and photostability, moreover, the PCE was observed to increase from 13.72% (3D) to 16.75% (3D/2D). Adding a 2D layer led to an

increase in the interfacial charge extraction and decreased recombination within the cell, due to reduced hysteresis. To date, the PCE for 2D/3D hybrid devices is in the range of 13-17%, showing promising results in terms of device longevity [32].

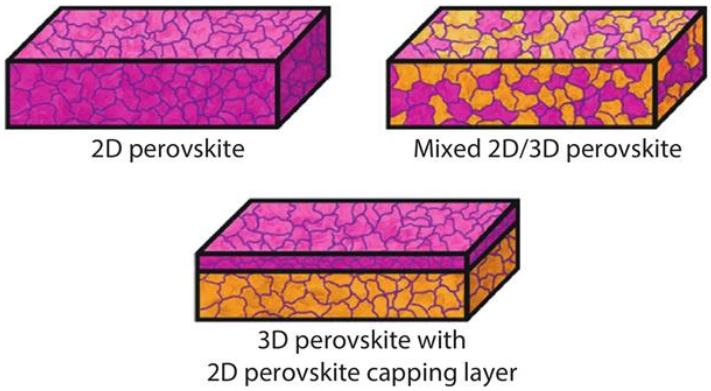

Figure 2-5: Examples of 2D HaP as the active layer of PSC [33].

Devices based on large-area single-crystal membranes that are synthesized using the optimized preparation methods are more promising for photoelectronic applications. To prove this, Wang *et al*. used an optimized fast-synthetic method to synthesise an inch scale quasi-2D HaP, $(C_4H_9NH_3)_n(CH_3NH_3)_{n-1}Pb_nI_{3n+1}$, single-crystal membranes that have uniform orientation and fast in-plane growth. These crystal membrane properties were found to be enabled by the spontaneous alignment of the alkylammonium cations and the chemical potentials for quasi-2D HaP single-crystal membranes. The growth of the 2D HaP occurred at the water-air interface. It was shown that the photodetectors with quasi-2D HaP single-crystal membranes have strikingly low dark current of $\sim 10^{-13}$ A, a higher on/off ratio of $\sim 10^4$, and faster response time achieved with the good thickness of $n = 1$ as compared to photodetectors with a quasi-2D HaP single-crystal membranes that has a good thickness of n greater than one [20]. Mei *et al.* incorporated a double layer of mesoporous TiO_2 and ZrO_2 scaffold that is infiltrated with a HaP and has no HTL. They produced the HaP $((5\text{-AVA})_n(MA)_{1-n}PbI_3)$ layer by drop-casting solutions of PbI_2, MA, and 5-AVAI through a porous carbon film. This HaP layer showed lower defect concentration and better pore filling as well as superior film growth at the mesoporous TiO_2/perovskite interface, which resulted in a significantly longer exciton lifetime and a higher quantum yield for photo-induced charge separation as compared to

$MAPbI_3$. The cell was found to produce a PCE of 12.8% and it was stable for >1000 h in ambient air under full sunlight [34].

Due to the reduced PCE during dimensional tailoring of a 3D HaP, the Cho group used a controlled layer-by-layer method to improve the PCE of their PSC. They fabricated a 3D/2D configuration using a controlled layer-by-layer growth of a PEA^+ containing 2D HaP that is on top of a mixed $Cs_{0.1}FA_{0.74}MA_{0.13}PbI_{2.48}Br_{0.39}$ HaP. To grow PEA^+ layer-by-layer, PEAI was spin-coated in an isopropanol solution on the mixed halide 3D HaP with excess PbI_2. They found that PEAI reacts in-situ with the excess PbI_2 to form a 2D HaP only on the top surface while the excess PbI_2 segregates on top of the 3D HaP. Interfacial charge carrier recombination and the PCE were found to increase >20% as the 2D HaP is present on top of the HTM. The HaP solar cells retained 85% of their PCE even under temperature conditions of 50 °C and illumination for 800 hours under 1 sun. [35]. These results provide insight into the possibility of enhancing the stability of the solar cell without affecting its PCE. Furthermore, Cho *et al*. recently achieved a PCE of ~20% by improving the water-repellent characteristics of a 3D/2D surface. They achieved this by fabricating a 2D HaP based on a fluorinated organic cation which imparts additional water-repellent properties to the thin active layer thin [36].

2.3.2 Using 2D HaP as the absorber layer

2D and mixed 2D/3D HaP as absorber layers, as well as placing a 2D HaP capping layer (*Figure 2-5*), could improve the stability and properties of HaP solar cells while taking advantage of the 2D material's hydrophobic nature. Smith *et al*. were the first to use 2D hybrid HaP as absorber layers in optoelectronic devices. In their work, PEA was used as an organic spacer (because it has a large ionic radius that is incompatible with a 3D HaP structure and facilitates the formation of a 2D layered structure) to synthesize n = 3 members of $(PEA)_2(MA)_{n-1}[Pb_nI_{3n+1}]$ HaP by combining (PEA: $C_6H_5(CH_2)_2NH_3^+$)I, (MA: $CH_3NH_2^+$)I, and PbI_2. Their findings showed the possibility of fabricating devices under humid conditions due to the enhanced resistivity of 2D HaP to moisture as compared to 3D $MAPbI_3$. During humid conditions (52% RH), a 3D MA HaP decomposes after 4-5 days, whereas a 2D HaP shows no changes after 46 days. They concluded that the low PCE (4.73%) for 2D HaP may be due to the inhibition of out-of-plane charge transport by organic cations and the fact that PEA acts as an insulating spacing layer between the conducting inorganic slabs [10].

Many organic spacers have been used to improve a 3D HaP absorber layer and the operation of solar cells. The addition of an organic spacer on the 3D HaP facilitated the formation of a 2D Ruddlesdern-Popper (RP) HaP. Cao *et al*. employed Butylamine (BA) because of its hydrophobic nature to fabricate a 2D $(CH_3(CH_2)_3NH_3)_2(CH_3NH_3)_{n-1}Pb_nI_{3n+1}$ (n = 1, 2, 3, and 4) HaP thin-film. They used PbI_2, MAI, and BA in a stoichiometric ratio that manifests the structural properties of a 2D (n = 1) and a 3D ($n = \infty$) HaP. They found that $MAPbI_3$ degraded and formed a yellow PbI_2 in a humid environment after a short time, but $(BA)_2(MA)_2Pb_3I_{10}$ remained stable under 40% humidity for after months. Even so, the 2D $(BA)_2(MA)_{n-1}Pb_nI_{3n+1}$ HaP only showed 5% PCE, which they attributed to the low absorption coefficient and poor transport [37]. Quan *et al*. reported on reduced-dimensionality (quasi-2D) HaP films that showed improved stability and maintained their high 3D HaP performance. They showed this by tuning the dimensionality of the HaP while adding PEAI organic molecules with different n values in the series $PEA_2(CH_3NH_3)_{n-1}Pb_nI_{3n+1}$. Their highest stability was achieved at n = 6, however, the performance was poor due to low mobility as shown in *Figure 2-6*. Under humid conditions (RH: 55%), after 3 days, the PCE of the 3D device decreased from 16.47% to 4.2%, while the PCEs of n = 60 and n = 40 devices decreased from 17.21% and 17.10% to 12.8% and 13.14% after 14 days, respectively[12].

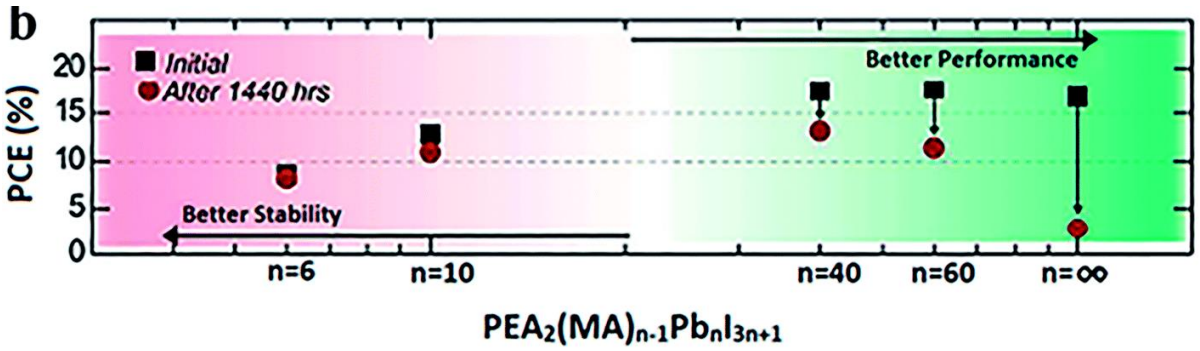

Figure 2-6: The PCEs of devices involving dimensionally tuned HaP [12].

Recently, Grancini *et al*. used a protonated salt of aminovaleric acid iodide ($HOOC(CH_2)_4NH_3I$, AVAI) as an organic precursor mixed with PbI_2 to engineer an ultra-stable 2D/3D $(HOOC(CH_2)_4NH_3)_2PbI_4/CH_3NH_3PbI_3$ HaP junction. They fabricated two 2D/3D HaP devices, one with an organic hole-transport-material (HTM) (using Au as an electrode), and the other without an HTM (using carbon electrode), they achieved a PCE of 14.6% and 11.2% for a 100 cm^2 module, respectively. The former, with a spiro HTM/Au contacts, retained up to 60% of its original PCE after 300 h of continuous illumination under argon atmosphere,

whereas a 3D $CH_3NH_3PbI_3$ device only retained 40% of its original PCE. The 2D/3D module without an HTM (containing carbon contact) was fully stable for >10 000h under 1 sun illumination at a constant temperature of 55 ℃ [11]. Iagher and Etgar fabricated three devices each containing a different organic spacer, including PEA, cyclohexylammonium iodide (CHMA), and benzylammonium iodide (BAI) in 2D/3D HaP structures, as well as including Cs. The addition of Cs to the structure led to an increase in PCE. However, the HaP solar cells containing 10 % Cs under encapsulation (both 3D $MAPbI_3$ and 2D/3D HaP) were not stable as compared to HaP solar cells without Cs cation under one sun illumination and humid conditions (RH: 30-50%) at a temperature of 50-60 ℃. According to their results, 2D/3D devices containing BA/Cs completely lost their performance under the mentioned conditions, whereas BAI-based 2D/3D HaP retained approximately 55% of PCE for 200 h. The stability behaviour of 2D/3D and 3D devices were not significantly different. The difference in ionic radii of Cs and Methylammonium (MA) in the absorber layer causes strains in the HaP solar cell, hindering its stability. These strains and distortions further accelerate perovskite degradation [38].

Due to the instability of the MA^+ organic cation, researchers are investigating the use of other organic cations that can occupy the A-site in the HaP and tailor these HaP into lower-dimensional HaP so that they can form stable 2D absorber layers. Nan *et al*. incorporated PEA^+ into $FAPbI_3$ HaP to fabricate a $FA_xPEA_{1-x}PbI_3$ which has an enhanced phase and ambient stability coupled with a high PCE [39]. $FA_xPEA_{1-x}PbI_3$ induced a self-assembled organic shell around the grain boundaries that raises the phase transition energy and phase stability while preventing moisture from reacting with the HaP. They reported that the blocked transport pathways and increased energy barrier of transition from a black photoactive phase into a yellow phase have been attributed to the presence of PEA^+ interlayer, which makes the black phase PEA-$FAPbI_3$ a kinetically stable substance. It was argued that the high PCE (17.71%) could be attributed to the surface passivation of PEA^+ in an inverted planar structure. In the case of unencapsulated devices, stored in air for 16 days under humid conditions (RH: 40%), for $FA_xPEA_{1-x}PbI_3$ (x = 40) and $FAPbI_3$, it was found that the former retained its initial PCE even after 16 days, while the latter lost all its PCE after 16 days [39]. Furthermore, Lee *et al*. used a 2D HaP (PEA_2PbI_4) to modify the crystallinity of the $FAPbI_3$ by incorporating the 2D into the precursor solution of $FAPbI_3$. They reported that the 2D HaP suppressed the non-HaP hexagonal phase and increased the carrier lifetime from 78.5 to 148.7 ns, indicating a decrease in defect density. This report is supported by the previous report from Nan *et al*. that passivation

occurs through the addition of a 2D HaP, resulting in a reduction of the grain boundaries that are moisture ingress pathways. Their results showed that unencapsulated devices stored in a desiccator (RH< 30%) under dark conditions degraded by 29% within 1392 h for $FAPbI_3$ whereas 2D-based devices lost 2% of their initial PCE at the same time interval. Maximum-Power-Point (MPP) tracking was used to determine the operational stability of the unencapsulated devices under one sun illumination, at ambient condition (RH: 50%) temperatures of 40 ℃. In these conditions, $FAPbI_3$ rapidly lost 68% of its PCE over 450 min, whereas 2D PEA_2PbI_4-based devices retained 80% of their PCE at the same time interval. With regards to encapsulated devices, $FAPbI_3$ retained 52,3% and the 2D/3D device retained 72.3% of their initial PCE after exposure to continuous light (0.9 sun; 90 ± 5 mW cm^{-2}, RH of 50%, and T = 40 °C) under open-circuit conditions for 500 h [40].

Researchers are also exploring the use of different cations to form 2D HaP absorber layers. Jiang *et al*. explored the sequel of using diammonium cation, ethylenediammonium (EDA^{2+}), on $(EDA)(MA)_2Pb_3I_{10}$. They found that EDA^{2+} is capable of forming twice as many hydrogen bonds with the inorganic layer as compared to a typical diammonium cation, and this improved the crystal quality and eventually the structure of the 2D HaP. The material delivered a maximum PCE of 11.58% when tested in an ambient environment after being encapsulation using UV-curable epoxy resin [41].

Apart from the quasi-2D HaP solar cells, there exist other types of 2D HaP, namely the Dion-Jacobson (DJ) HaP and the HaP with alternating cations in the interlayer space (ACI) as shown in *Figure 2-7*. The DJ HaP are known to have the inorganic layers stacked on top of each other and are represented by the formula $RA_{n-1}B_nX_{3n+1}$, whereas the ACI HaP are known to contain the layer-stacking characteristics of both the DJ and RP structures. Layer stacking within the ACI due to the A cation residing in and filling the lead halide sheets and the interlayer along with the R cation. These ACI HaP are represented by the formula $RA_nB_nX_{3n+1}$.

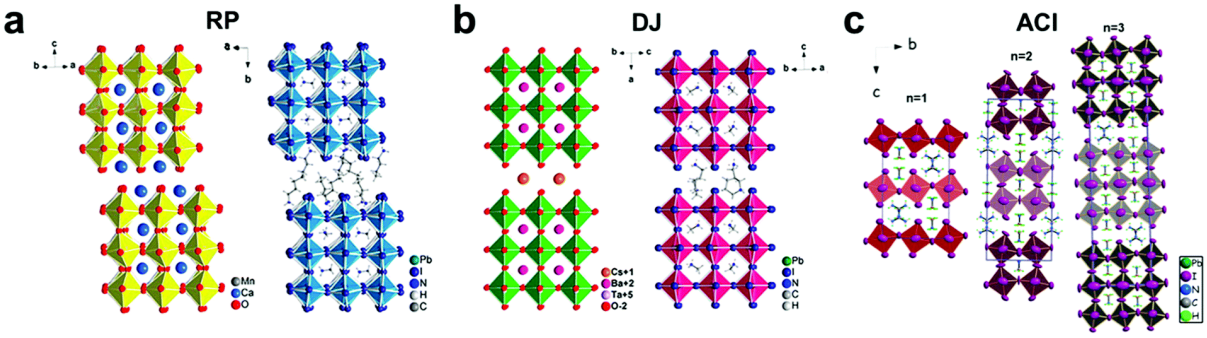

Figure 2-7: Differences between RP, DJ, and ACI phase 2D HaP structures [42].

In 2016, Hojamberdiev *et al.* reported on the fabrication of a DJ three-layer HaP phase $CsBa_2Ta_3O_{10}$ crystal using the conventional solid-state reaction. Besides these reactions, nitridation-protonation-intercalation-exfoliation was used to synthesise the nitrided $Ba_2Ta_3O_{10}$ nanosheets. The research proved that the 2D DJ HaP can be used for visible-driven photocatalytic water-splitting applications [43]. Similarly, Mao *et al*. presented the first complete homologous series of hybrid 2D HaP that adopt the DJ structure for solar cell applications [44]. In their work, they used two types of R cations, 3-(aminomethyl)piperidinium (3AMP) and 4-(aminomethyl)piperidinium (4AMP), to fabricate $(3AMP)(MA)_3Pb_4I_{13}$ and $(4AMP)(MA)_3Pb_4I_{13}$ HaP, respectively, which were referred to as the lead iodide DJ HaP. The 3AMP series contained a smaller bandgap than the 4AMP series. The shift in bandgap shift is said to have been caused by the indirect influence of the organic cation on the inorganic framework. As these materials were used as light absorbers, the $(3AMP)(MA)_3Pb_4I_{13}$ HaP showed a PCE of 7.32%, which was higher than the of $(4AMP)(MA)_3Pb_4I_{13}$. In another study, Li *et al*. applied a step-cooling method to modify the position of $CH_2NH_3^+$ in 4-(aminomethyl)pyridinium (4AMPY) to obtain a 3-(aminomethyl)pyridinium (3AMPY) for photovoltaic applications. They observed the stacking of the inorganic layers changed from an eclipsed to a slightly offset configuration, and the bandgap was smaller for 3AMPY series than for 4AMPY series due to the octahedra tilts between the two series. The 3AMPY produced a higher PCE (9.2%) than 4AMPY absorber layer [45]. Also, using an aromatic ring instead of an aliphatic ring of the same size introduces new features. These features include a rise in the dielectric constant of the interlayer space, an increase in the rigidity of the cation, and a greater delocalization of the positive charge on the aromatic ring. Another research was done by Liang *et al*. were a new layered DJ $KSr_2Nb_3O_{10}$ HaP consisting of two protonated niobates, $HSr_2Nb_3O_{10}{\cdot}1.2H_2O$ and $HSr_2Nb_3O_{10}$, was discovered. The niobates were derived from the DJ HaP with a triple slab represented by the

general formula $M[A_{n-1}Nb_nO_{3n+1}]$ where n=3 [46]. They reported that the niobates are a result of $[Sr_2Nb_3O_{10}]^-$ interleaved with K^+, H_3O^+, or H^+.

On the other hand, ACI HaP have only reported the use of the guanidinium (Gau^+) cation in the formation of ACI structures. Gua^+ is used in ACI HaP because it can stabilize the HaP structure by alternating ordering its cations with the methylammonium cations in the interlayer space. Recently, Zhang *et al.* used the ACI $(Gau)(MA)_nPb_nI_{3n+1}$ HaP to investigate how a dynamical process can affect the resulting thin film and how this HaP can be applied in photovoltaics. They used antisolvent engineering and hot-casting techniques as dynamic processes. Techniques such as these were crucial to controlling the kinetic transformations from the sol-gel phase to the crystalline phase. A 2D GA_2PbI_4 was identified as the key intermediate phase that was influenced by the deposition technique. Using transient absorption spectroscopy, they confirmed the presence of internal charge transfer between different n phases. A PCE of 14.7% was achieved in planer solar cells and long-term stability was achieved as compared to a 3D $MAPbI_3$ [47]. Soe *et al*. reported on the ACI $(C(NH_2)_3)(CH_3NH_3)_nPb_nI_{3n+1}$ 2D HaP with n = 3 for solar cell application. To synthesise this HaP, an antisolvent dripping method was used, where the delay-time for dripping the antisolvent chlorobenzene was varied. A monotonic decrease in the optical bandgap was observed when n increases, which conveys narrower gaps as opposed to the corresponding RP HaP. This led to the conclusion that the ACI HaP are direct bandgap semiconductors with wide valence and conduction bandwidths. Their photovoltaic devices which contained the ACI HaP films resulted in a PCE of 7.26% [42]. Transition metal dichalcogenide (TMD) [48], hexagonal boron nitride (*h*BN) [49], graphdiyne (GD) [50], and black phosphorus (BP) [51] are some of the new 2D materials which emerged after the discovery of single-atom layered graphene. These 2D materials are known to have mechanical flexibility, superior surface sensitivity, interesting quantum effects in heterostructures, and achievable stacking modes by van der Waals forces 2D HaP in light-emitting diodes

The 2D HaP have also proven to have applications in perovskite light-emitting diodes (PeLEDs) due to their efficient and narrow emission. Pure 2D and quasi-2D HaP containing the RP-type of layered structure are known to enlarge the exciton binding energy and confine the charge carriers, and these are characteristics that are considered for efficient LEDs. However, a mixture of phases including the phase impurity exists in the quasi-2D perovskites and this results in low emission efficiencies. The addition conversion of a 3D into a quasi-2D

HaP introduces more defects on the surface or at the grain boundaries of the quasi-2D, this is due to the decrease in the crystal sizes. To combat this setback, Yang *et al*. fabricated a 2D ($PEA_2(FAPbBr_3)_{n-1}PbBr_4$ (n = 1, 2, …, ∞) and investigated the effects of trioctlyphosphine oxide (TOPO). They found that they found that the PeLED based on $PEA_2(FAPbBr_3)_{n-1}PbBr_4$ (where n=3) results in a current efficiency of 62.4 cd A^{-1} and external quantum efficiency (EQE) of 14.36%. Their HaP (where n=3) showed a high Photoluminescence, however, this material contains a mixture of phases and phase impurities, thus causing a low emission efficiency [61]. Whereas, Chu *et al.* added a large cation ($CH_3CH_2NH_2$) into the Cs^+ site in $PEA_2(CsPbBr_3)_2PbBr_4$ HaP. The addition of the large cation resulted in a decrease in the Pb-Br orbit coupling and an increase in the bandgap for blue emission. A PL shift from a green region (508 nm) to a blue region (466 nm) was observed. They concluded that from the X-ray diffraction and nuclear magnetic resonance the Cs+ cation was successfully replaced to form $PEA_2(Cs_{1-x}EA_xPbBr_3)_2PbBr_4$. Through the optimization of the content of $PEA_2(CsPbBr_3)_2PbBr_4$, an EQE of 12.1% was achieved when 60% of the large cation was added and over 70% of the quantum yield was successfully obtained and the emission spectra were found to be stable under thermal stress and light [62].

2.3.3 Lead-free 2D HaP

When Lead (Pb) comes into contact with water or humid air, it forms a water-soluble compound that can accumulate in the food chains and eventually pass through the food chain into the bloodstream [63]. Due to the toxic nature of lead in the environment, other research groups are exploring the fabrication of 2D lead-free HaP cells. Sn^{2+} has been used to replace Pb^{2+} in a quasi-2D HaP that included a bulky heterojunction film of $PEA_2FA_{n-1}Sn_nI_{3n+1}$. When the 2D phase and 3D phase were mixed, the 2D phase sank to the bottom of the 3D phase, forming an oriented layer structure. A compact pinhole-free film, which blocks the diffusion of oxygen into the HaP lattice is formed as the PEA^+ locates itself at the boundaries of the 3D HaP grains, and this improves the stability of the cell in comparison with the pure 3D HaP [3]. Furthermore, the highly oriented films enhanced charge carrier transport when grown in a perpendicular direction. A PCE of <6% was achieved with enhanced stability that was sustained for 100 h under nitrogen. Cao D *et al.* fabricated $BA_2MA_{n-1}Sn_nI_{3n+1}$ based solar cells with a PCE of 2.5% for $n = 4$ and these HaP were stable for >1 month when encapsulated [64]. Histoammonium (HA^{2+}) and benzylammonium (BA^{2+}) were varied while forming $HAPb_{1-x}Sn_xI_4$ and $BA_2Pb_{1-x}Sn_xI_4$ [63]. The single-layered 2D $HAPb_{1-x}Sn_xI_4$ and $BA_2Pb_{1-x}Sn_xI_4$

HaP are less distorted than many 2D Pb-based HaP frameworks, resulting in a smaller bandgap [63]. For example, the $HASnI_4$ and $HAPbI_4$ have bandgaps of 1.67 and 2.05 eV, respectively.

Shen *et al*. synthesized a layered structure of 2D $(PEA)_2CsSn_2I_7$ via mechanical exfoliation, and then tuned it to establish smooth surfaces on microdevices containing exfoliated flakes. To fabricate microplate electronic devices with high conductivity and high field-effect hole mobility of 34 $cm^2\ V^{-1}\ s^{-1}$, they transferred the exfoliated $(PEA)_2CsSn_2I_7$ thin-flakes to a presynthesized double probe electrode. They also discovered that this method provides difficulty in controlling the fragmentation process and obtaining HaP nanosheets with controllable layers and sizes. After that, the Maksym V. Kavalenko group reported on the thermal injection of nanoplatelets into the device. They found that this method can be used to carefully adjust the thickness of the platelets [65].

Several researchers have explored the use of Bismuth as a substitute for toxic lead because of its non-toxic and stability. In one study, colloidal bismuth-based 2D HaP, $Cs_3Bi_2Br_9$ with the unit cell shown in *Figure 2-8*, was prepared by injecting cesium oleate into a mixture of 1-octadecene, bismuth tribromide, and oleic acid at elevated temperature using classic injection technology. The $Cs_3Bi_2Br_9$ nanoplatelets were found to display a parallelogram layered structure and each of the layers is made up of two Bi-Br octahedral layers, as mentioned by Lian *et al*. They reported that the length of the nanosheets varied from 60 to 250 nm, and their thickness is uniform at ~ 9 nm [66]. To regulate the halogen ions in the HaP crystals, an ion-exchange reaction was used. They concluded that it is difficult to prepare larger thin layers using colloidal methods because the films tend to fracture or aggregate in colloidal suspensions.

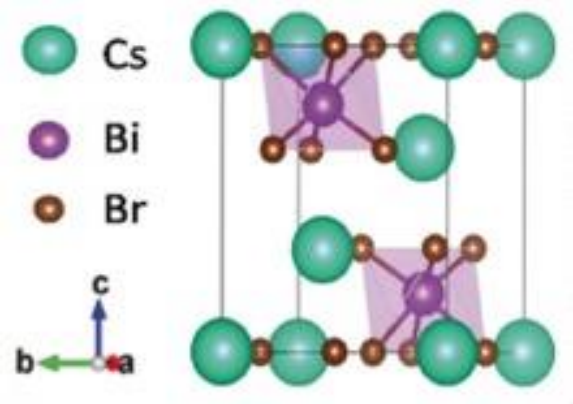

Figure 2-8: Unit cell of $Cs_3Bi_2Br_9$ [66].

Solution processing is the most widely used method in lead-free HaP owing to its advantages and ease of use compared to the other two methods. Mitzi D *et al*. used the solution processing method to synthesize a family of organic layered Sn-based HaP, $(C_4H_9NH_3)_2(CH_3NH_3)_{n-1}Sn_nI_{3n+1}$ (n = 1–5) and showed that modulating the organic layer can affect the electrical properties of halide HaP nanosheets. Their results showed that the plate-like crystals are single crystals for n = 1-4 and pure for n = 5 [67]. Chen *et al*. used the solution processing method to report on the synthesis and photovoltaic properties of low-dimensional Dion–Jacobson Sn-based HaP, $(4AMP)(FA)_{n-1}Sn_nI_{3n+1}$ (4AMP is 4-(aminomethyl)piperidinium) as means of overcoming the oxidation of Sn^{2+} [68]. Their results showed that an increase in n values is followed by a systematic red-shift in the absorption edge and the PL peaks of the material, and a change from 2D to quasi-2D is observed. They observed an 18.56 ns PL lifetime for Sn-based HaP materials as well.

2.3.4 Charge transport in 2D HaP solar cell

To overcome the challenges associated with charge transport in 2D structures, it is necessary to improve the orientation of a 2D HaP by growing single-crystalline materials, as proposed by Tsai *et al*. [69]. They used a hot casting process to produce uniform RP phase-layered 2D HaP films that have aligned crystalline planes with the out-of-plane orientation. In this way, charge transport along the HaP planes was observed to be efficient. Using this method, they achieved a PCE of 12.52%, with or without encapsulation, $(BA)_2(MA)_3Pb_4I_{13}$ produced outstanding photo and moisture stability as compared to 3D HaP devices. Under one-sun illumination, it was observed that an unencapsulated 2D HaP device maintained 80% of its initial PCE after 200 h, and after 2050 h, it had degraded to approximately 70% of its initial PCE. When the same conditions of one-sun illumination were applied, the 3D HaP device retained only 40% of its initial PCE within 24 h and then degraded to <10% of its initial PCE after 2050 h. Furthermore, they tested the stability of the encapsulated devices under one sun illumination and at humid conditions (RH: 65%) for 2250 h. The results showed that the 3D HaP device lost more than 50% of its original performance after 10 h and then reached saturation at 10% of its original PCE value after 800 h, whereas a 2D HaP device showed no degradation over 2250 h under light illumination [69].

Chen *et al.* also used the hot casting method but instead of using n-BA^+ as an organic spacer, they used a short branched-chain butylamine (iso-BA) to form a 2D HaP. They

compared the results obtained at room temperature and the results attained by a hot casting method. The results show that at room temperature (iso-$BA)_2(MA)_3Pb_4I_{13}$ reveals a remarkable crystallinity and an improved out-of-plane orientation, with an enhanced charged mobility and charge transport as compared to (n-$BA)_2(MA)_3Pb_4I_{13}$. In contrast, the 2D HaP show more ambient stability when prepared using the hot cast method, since they retained their initial absorption after storage under humid conditions (RH: 60%) at 20 ℃ for 840 h. The highest PCE (10.63%) was achieved by using a hot casting method for (iso-$BA)_2(MA)_3Pb_4I_{13}$ [70], however, the stability of the complete device was not reported. BA molecules were also studied in another study where 5% Cs was added to the 2D $(BA)_2Cs_{3x}(MA)_{3-3x}Pb_4I_{13}$ lattice. Results showed a remarkable improvement in both moisture content and device stability, as well as an improvement in PCE from 12.3% to 13.7%. After 1400h, it was observed that the Cs_5-2D devices retain 89% of their initial PCE under ambient conditions (RH: 30%), whereas Cs_0-2D devices, under the same conditions, retained 74%. They found that when 2D $(BA)_2(MA)_3Pb_4I_{13}$ are doped with Cs^+ the resulting devices correspond efficiently with their more stable phase structures and more hydrophobic surfaces. To improve the stability and PCE, Zhang *et al*. used a crystallographic orientation method to synthesize a 2D $(BA)_2(MA)_{n-1}Pb_nI_{3n+1}$ HaP solar cell. To achieve this, a small amount of ammonium thiocyanate (NH_4SCN) was added to the HaP precursor solution ($BAI : MAI : PbI_2 : NH_4SCN = 2 : 2 : 3 : 1$). This solution mixture produced vertically oriented perovskites based on the $(BA)_2(MA)_2Pb_3I_{10}$ molecule, resulting in devices having an average PCE, for n = 3 and n = 4, of 6.82% and 8.79%, respectively. Adding NH_4SCN led to reduced grain boundaries in the direction perpendicular to the substrate. Under 1 sun illumination of the thermally annealed 2D $(BA)_2(MA)_2Pb_3I_{10}$-based HaP solar cell, the PCE was retained for over 600 s. But when the device was kept under a purified N_2 glove box, its PCE remains unchanged for almost 25 days [71].

The weak binding energy between electrons and holes is most favourable for charge carriers to be easily separated and transported towards their respective collectors in an ideal solar cell. Thus, control over the exciton binding energy is required in the 2D RP HaP to enable their applications in a broad range of optoelectronic technologies. Smith *et al*. studied the intercalation of I_2 in alkyl HaP ($(C_6)_2[PbI_4]$) and iodoalkyl HaP ($(IC_6)_2[PbI_4]\cdot 2I_2$) to demonstrate that the insertion of small molecules into the binding spacers can significantly reduce the electronic confinement in 2D RP HaP [72]. And they also showed that the I_2 intercalation could lead to more polarizable organic layers as compared to the inorganic layers [72]. After the work done by Yang *et al.* in their report on the HaP degradation process, they

did more work on the solar cell and found that the identity of the hole transport layer plays a role in the stability of the underlying HaP film. They concluded that this suggests a route towards HaP solar cells that has a longer device lifetime as well as resistance to humidity [73]. This conclusion was based on the presence/absence of the lithium bis(trifluoro-methanesulfonyl)imide (Li-TFSI) dopant in 2,20,7,70-tetrakis(N,Ndi-4-methoxyphenylamino)-9,90-spirobifluorene (Spiro-OMeTAD), poly[bis(4-phenyl)(2,4,6-trimethylphenyl)-amine] (PTAA), and poly(3-hexylthiophene) (P3HT). The identity of the HTL with Li-TFSI dopant was found to affect its ability to protect the underlying HaP film. For Spiro-OMeTAD, the presence of Li-TFSI accelerated the decomposition process of the HaP film, whereas the PTAA and P3HT appeared to act as barriers to moisture ingress. The absence of Li-TFSI on Spiro-OMeTAD and PTAA showed a sharp discontinuity in the absorbance data, after which the rate of decomposition increased dramatically. However, the P3HT-coated films were stable for a day before showing any signs of decomposition [73].

Different types and sizes of the organic cation molecules used as 2D absorber layers produce different responses from solar cells. Safdari *et al*. demonstrated this by synthesizing a pure 2D HaP using diammonium cations containing different organic chain lengths [74]. Based on the reaction between PbI_2 and various di-cations, such as 1,4-diaminobutane, 1,6-diaminohexane, and 1,8-diaminooctane, different 2D HaP were produced, including $[NH_3(CH_2)_4NH_3]PbI_4$ ($BdAPbI_4$), $[NH_3(CH_2)_6NH_3]PbI_4$ ($HdAPbI_4$), and $[NH_3(CH_2)_8NH_3]PbI_4$ ($OdAPbI_4$), respectively with different band energies as shown in *Figure 2-9*. In their study, they concluded that the bulkier the cation used, the less it could be used for solar cell applications due to reduced charge transport characteristics, but excellent results were observed when using $BdAPbI_4$ and $HdAPbI_4$ with no phase transition for temperatures of up to 200 °C. For $BdAPbI_4$-based devices, however, they observed a low PCE of 1.082%, which was slightly similar to the PCE of 2.1% for $MAPbI_3$ fabricated under humid conditions (RH: 55.6%). The insulating nature of organic spacers poses a great challenge of hindering charge transport. The size and distance between Pb-I structural units in a material are reduced by adding a bulky cation on $MAPbI_3$, but consequently, this reduces the electrical conductivity of the material [74, 75]. In 3D $MAPbI_3$, the conductivity was measured to be 1.1×10^{-4} S cm^{-1}, while in 1D $(CH_3CH_2NH_3)PbI_3$, it is 1.3×10^{-6} S cm^{-1} [74].

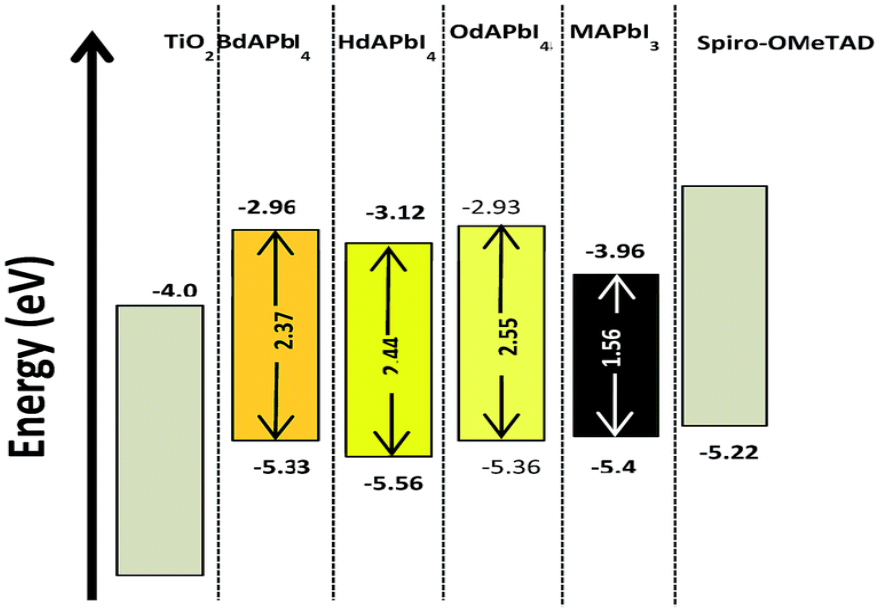

Figure 2-9: Band energy diagrams of the 2D HaP materials compared to other components of the solar cells [74].

Polymer cations can also be used in 2D HaP as an alternative to small-molecule cations since they can improve the film's quality and prevent moisture from diffusing into the HaP layer. In contrast to 2D HaP containing a small molecule of bulky ammonium, the polymer cations can improve charge transport within the device as a result of induced tight stacking of separated inorganic unit layers. In this regard, Zou *et al.* demonstrated the use of polymers with coordinating groups to improve the performance of a solution-processed semiconductor film. They proposed that the binding interactions between a polymer and a HaP affect passivation, so they tested this by using polymers that have different functional groups on $MAPbI_3$. Branched polyethyleneimine (b-PEI) was chosen for its amino groups, polyvinylpyridine (PVP) for its Lewis base pyridine groups, and polyacrylic acid (PAA) for its carboxylic acids. They found that the HaP solar cell treated with PVP has a long shelf life of up to 90 days (retaining 85% of the initial efficiency) [76]. In contrast, Yao *et al*. synthesized a 2D $(PEI)_2(MA)_{n-1}Pb_nI_{3n+1}$ (n = 3, 5, 7) HaP by using polyethylenimine (PEI) cations. The authors claimed that the assumption that the hydrophobic polymeric-ammonium can present stronger steric hindrance, thereby improving moisture stability of the HaP crystals and also forming a more compact HaP film that can prevent water molecules from diffusing into HaP layer. A maximum PCE of 10.08% was achieved for the $(PEI)_2(MA)_6Pb_7I_{22}$-based device, which was much better than the photovoltaic parameter of the $(BA)_2(MA)_6Pb_7I_{22}$ PSC device. In an actual sense, superior charge transport properties are achieved through the use of polymeric-

ammonium cations since they are capable of covalently linking the adjoining HaP layers. The performance loss in 2D solar cells was observed to be lower than the large area 3D HaP devices. 3D $MAPbI_3$ decomposed immediately in humid conditions (RH: 50%), whereas no noticeable changes were observed in $(PEI)_2(MA)_{n-1}Pb_nI_{3n+1}$ for more than a month. Also, the $(PEI)_2(MA)_6Pb_7I_{22}$ and $(PEI)_2(MA)_4Pb_5I_{16}$ based devices retain PCE values after 500 hours in light [77].

2.3.5 HaP trap states

The presence of trapping centers, which reduce the effectiveness of charge collection in a solar cell or a detector, is one of the most important aspects affecting the performance of multifunctional HaP devices. Energy levels in the bandgap are created by centers trapped in a semiconductor lattice. These energy states trap free carriers throughout their relaxation process, which negatively affects the free charge transport parameters like lifetime and drift mobility. It is quite difficult to identify these traps and the relaxation dynamics that go along with them. Because the optical and thermal transition energies of traps in semiconductors differ, the overwhelming nonradiative nature of these energy transitions prevents the detection of crucial factors associated to trapping/detrapping by optical spectroscopies, including photoluminescence [9]. Additionally, the substantial Urbach tail absorption prevents optical spectroscopies from detecting shallow traps with energies Et 0.3 eV. [11]. The low activation energy of shallow traps can impose limitations on other methods, such as thermal emission. Multiple phase transitions in HaP additionally prohibit the sample from being sufficiently cooled to allow thermal relaxation of the traps to expose the traps' characteristics.

Beyond the traditional paradigm of trap-controlled mobility, it is known that the projected numerous trapping states in the bandgap of HaP complicate the dynamics of charge transport [17]. The effective mobility model, as it is often known, takes into account a semiconductor with a single trap that delays free charge carriers. In order to clearly characterize the dynamics of free charge carrier transport in HaP semiconductors, a novel strategy is required.

To do this, Musiienko et al., followed the center of the charge cloud that is impacted by traps using Monte Carlo (MC) simulations to analyze the delay of charge carriers and determine the effective transit time. The notion of effective mobility (effh) is then revised in light of effective transit time. They hypothesised that they can examine the charge transport characteristics of

any semiconductor with any number of active traps using such a method. Finally, they examined how traps affect the effective mobility of carriers (holes) in HaP devices and how it relates to temperature, thickness, and the electric field. They also investigated the impact of traps on the mobility-lifetime product to show the impact of traps on the performance of $MAPbBr_3$ single-crystal devices. To manage traps and enhance OMHP device performance, it is essential to understand how they affect charge transport qualities. They observed that free holes trap and detrap at speeds between a few and hundreds of microseconds. In contrast to earlier investigations, their findings showed a significant detrapping activity of traps. They demonstrated how these traps have a significant impact on $MAPbBr_3$'s transport properties, including mobility and mobility-lifetime product.

2.3.5 Degradation in 2D HaP thin films

The photovoltaic devices are affected by intrinsic and extrinsic factors in the HaP material. Intrinsic factors include ionic properties, such as ion migration, as well as the composition of the HaP material [78]. Whilst, extrinsic factors include moisture, heat, and oxygen, amongst other factors [79]. The degradation process of the HaP material is accelerated by the presence of light and oxygen. Due to the presence of light and oxygen, moisture has been considered the most important factor that affects the stability of the HaP material [80]. The activation energy of ion migration inside the HaP crystal is low and the molecular dissociation, including ion migration, are liable to occur in the structure, this restricts the structural stability of the HaP materials and thus results in the degradation of the film [81]. The organic-inorganic HaP materials are semiconductors with exceptional optical and electrical properties such as strong optical absorption, high carrier mobility, and small exciton binding energy [82]. Yang *et al.* reported on the HaP degradation process by using in-situ absorption spectroscopy and in-situ grazing incidence X-ray diffraction to monitor the phase change in the HaP degradation process. They demonstrated the formation of a hydrated intermediate that contains an isolated PbI_6^{4-} octahedra as the first step of the degradation mechanism in $CH_3NH_3PbI_3$ [73].

HaP are promising new materials when used in solar cells, however, the presence of moisture affects their chemical stability. Quasi-2D HaP that incorporates hydrophobic organic interlayers' presence improved resistance to degradation by moisture, but this affects the overall efficiency of the cell. To illuminate the factors that affect the optoelectronic properties

of these materials, Milot *et al*. investigated the charge transport properties and crystallographic orientation of mixed MA-PEAPbI_3 thin films as a function of the MA-to-PEA ratios, including the thickness of the encapsulated MA lead-halide layers [83]. They found that trap passivation highly influences the monomolecular charge-carrier recombination rates. The monomolecular charge-carrier recombination rates first decreased with increasing PEA fraction, but then increased significantly as excitonic effects began to dominate for thin confined layers. The density of states for electronic transitions is altered by the bimolecular and Auger recombination rate constants due to their sensitivity to the changes in electronic confinement [83].

Light exposure in a 3D HaP lead to the breaking of C-N bonds in MA^+, which creates methane and ammonia gas, whilst part of the residual PbI_2X forms a metallic Pb in the film, as reported by Xu *et al* [84]. Bulky ammonium substituted for MA+ enhances crystal quality, reduces defect densities, improves light resistance, and eliminates these issues. Recent work by Fang and Peddesseau *et al*. has demonstrated that light-induced degradation can also occur and distorts the 2D HaP lattice. Organic cations and HI are released as by-products during the degradation of the material, typically from the edges of the 2D crystal and the surfaces at the organic/inorganic interfaces [27, 85]. The controlled growth of large and high-quality crystals would minimize these effects. Chen *et al*. used the solution-processing method to control the crystal growth with a vertical alignment of a 2D $BA_2MA_3Pb_4I_{13}$ HaP and also convey directional charge transport on the inorganic backbone. Monitoring the liquid/air interface allowed them to control nucleation and growth of the 2D HaP during the deposition of the solution. Their suggestion was to pre-crystalize the HaP during the annealing step at high temperatures on a hotplate for a short time. This was done with the least spin-induced convection to acquire a high level of control of the HaP growth whilst applying a thermal gradient during the spinning step. The resulting 2D HaP film had a vertical orientation with a thickness of 325nm and it surpassed the films with partial random orientation. Their results showed a higher short-circuit current density with a PCE of 9.7 % [86]. Tsai *et al*. used the same method as Chan *et al.* but changed the thickness of the $BA_2MA_3Pb_4I_{13}$ HaP to ~200nm. With this thickness they managed to achieve a PCE of 11%, thus they concluded that this is the optimal thickness to be used for $BA_2MA_3Pb_4I_{13}$ HaP [87].

2.3.8. Solar Energy Technologies for Generation of Electricity

Concentrated photovoltaic systems focus sunlight from a large area onto a small blackened receiver. This greatly increases the intensity of the light and makes it possible to generate high temperatures. Arrays of well-aligned mirrors or lenses (shown in) can focus enough sunlight to heat a subject to temperatures of 2,000 °C (3,600 °F) or higher. This heat can then be used to power a steam turbine electric generator power plant by operating a boiler, which generates steam. The moveable mirrors can be set to concentrate huge amounts of solar radiation onto blackened pipes through which water is pumped and therefore heated to produce steam directly.

2.4 REFERENCES

1. Green, M., et al., *Solar cell efficiency tables (version 57).* Progress in photovoltaics: research and applications, 2021. **29**(1): p. 3-15.
2. Ma, C., et al., *2D/3D perovskite hybrids as moisture-tolerant and efficient light absorbers for solar cells.* Nanoscale, 2016. **8**(43): p. 18309-18314.
3. Ran, C., et al., *Bilateral interface engineering toward efficient 2D–3D bulk heterojunction tin halide lead-free perovskite solar cells.* ACS Energy Letters, 2018. **3**(3): p. 713-721.
4. Galagan, Y., et al., *Towards the scaling up of perovskite solar cells and modules.* Journal of Materials Chemistry A, 2016. **4**(15): p. 5700-5705.
5. Li, Z., et al., *Stabilizing perovskite structures by tuning tolerance factor: formation of formamidinium and cesium lead iodide solid-state alloys.* Chemistry of Materials, 2015. **28**(1): p. 284-292.
6. Ahmad, Z., et al., *Instability in CH 3 NH 3 PbI 3 perovskite solar cells due to elemental migration and chemical composition changes.* Scientific reports, 2017. **7**(1): p. 1-8.
7. Dodabalapur, A., L. Torsi, and H. Katz, *Organic transistors: two-dimensional transport and improved electrical characteristics.* Science, 1995. **268**(5208): p. 270-271.
8. Even, J., L. Pedesseau, and C. Katan, *Understanding quantum confinement of charge carriers in layered 2D hybrid perovskites.* ChemPhysChem, 2014. **15**(17): p. 3733-3741.
9. Mitzi, D., et al., *Conducting layered organic-inorganic halides containing< 110>-oriented perovskite sheets.* Science, 1995. **267**(5203): p. 1473-1476.
10. Smith, I.C., et al., *A layered hybrid perovskite solar-cell absorber with enhanced moisture stability.* Angewandte Chemie International Edition, 2014. **53**(42): p. 11232-11235.
11. Grancini, G., et al., *One-Year stable perovskite solar cells by 2D/3D interface engineering.* Nature communications, 2017. **8**: p. 15684.
12. Quan, L.N., et al., *Ligand-stabilized reduced-dimensionality perovskites.* Journal of the American Chemical Society, 2016. **138**(8): p. 2649-2655.
13. Du, K.-z., et al., *Two-dimensional lead (II) halide-based hybrid perovskites templated by acene alkylamines: crystal structures, optical properties, and piezoelectricity.* Inorganic chemistry, 2017. **56**(15): p. 9291-9302.
14. Mitzi, D.B., *A layered solution crystal growth technique and the crystal structure of (C6H5C2H4NH3) 2PbCl4.* Journal of Solid State Chemistry, 1999. **145**(2): p. 694-704.
15. Grancini, G. and M.K. Nazeeruddin, *Dimensional tailoring of hybrid perovskites for photovoltaics.* Nature Reviews Materials, 2019. **4**(1): p. 4-22.
16. Gao, P., M. Grätzel, and M.K. Nazeeruddin, *Organohalide lead perovskites for photovoltaic applications.* Energy & Environmental Science, 2014. **7**(8): p. 2448-2463.
17. Habisreutinger, S.N., et al., *Carbon nanotube/polymer composites as a highly stable hole collection layer in perovskite solar cells.* Nano letters, 2014. **14**(10): p. 5561-5568.
18. Gan, X., et al., *2D homologous organic-inorganic hybrids as light-absorbers for planer and nanorod-based perovskite solar cells.* Solar Energy Materials and Solar Cells, 2017. **162**: p. 93-102.

19. Chen, M., et al., *Enhanced efficiency and stability of perovskite solar cells by 2D perovskite vapor-assisted interface optimization.* Journal of Energy Chemistry, 2020. **45**: p. 103-109.
20. Wang, K., et al., *Quasi-two-dimensional halide perovskite single crystal photodetector.* ACS nano, 2018. **12**(5): p. 4919-4929.
21. Dhanabalan, B., et al., *Simple fabrication of layered halide perovskite platelets and enhanced photoluminescence from mechanically exfoliated flakes.* Nanoscale, 2019. **11**(17): p. 8334-8342.
22. Dou, L., et al., *Atomically thin two-dimensional organic-inorganic hybrid perovskites.* Science, 2015. **349**(6255): p. 1518-1521.
23. Tafazoli, S., et al., *The role of a vapor-assisted solution process on tailoring the chemical composition and morphology of mixed-halide perovskite solar cells.* CrystEngComm, 2018. **20**(31): p. 4428-4435.
24. Rong, L.-Y., et al., *2D perovskite hybrid with both semiconductive and yellow light emission properties.* Inorganic Chemistry Communications, 2019. **102**: p. 90-94.
25. Ma, C., et al., *2D Perovskites with Short Interlayer Distance for High-Performance Solar Cell Application.* Advanced Materials, 2018. **30**(22): p. 1800710.
26. Koh, T.M., et al., *Nanostructuring mixed-dimensional perovskites: a route toward tunable, efficient photovoltaics.* Advanced Materials, 2016. **28**(19): p. 3653-3661.
27. Fang, H.H., et al., *Unravelling Light-Induced Degradation of Layered Perovskite Crystals and Design of Efficient Encapsulation for Improved Photostability.* Advanced Functional Materials, 2018. **28**(21): p. 1800305.
28. Shi, D., et al., *Low trap-state density and long carrier diffusion in organolead trihalide perovskite single crystals.* Science, 2015. **347**(6221): p. 519-522.
29. Yang, J., et al., *Effects of aromatic ammoniums on methyl ammonium lead iodide hybrid perovskite materials.* Journal of Nanomaterials, 2017. **2017**.
30. Yao, K., et al., *A general fabrication procedure for efficient and stable planar perovskite solar cells: Morphological and interfacial control by in-situ-generated layered perovskite.* Nano Energy, 2015. **18**: p. 165-175.
31. Yao, K., et al., *Mixed perovskite based on methyl-ammonium and polymeric-ammonium for stable and reproducible solar cells.* Chemical Communications, 2015. **51**(84): p. 15430-15433.
32. Chen, J., J.Y. Seo, and N.G. Park, *Simultaneous improvement of photovoltaic performance and stability by in situ formation of 2D perovskite at (FAPbI3) 0.88 (CsPbBr3) 0.12/CuSCN interface.* Advanced Energy Materials, 2018. **8**(12): p. 1702714.
33. Ortiz-Cervantes, C., P. Carmona-Monroy, and D. Solis-Ibarra, *Two-Dimensional Halide Perovskites in Solar Cells: 2D or not 2D?* ChemSusChem, 2019. **12**(8): p. 1560-1575.
34. Mei, A., et al., *A hole-conductor–free, fully printable mesoscopic perovskite solar cell with high stability.* science, 2014. **345**(6194): p. 295-298.
35. Cho, K.T., et al., *Selective growth of layered perovskites for stable and efficient photovoltaics.* Energy & Environmental Science, 2018. **11**(4): p. 952-959.
36. Cho, K.T., et al., *Water-repellent low-dimensional fluorous perovskite as interfacial coating for 20% efficient solar cells.* Nano letters, 2018. **18**(9): p. 5467-5474.
37. Cao, D.H., et al., *2D homologous perovskites as light-absorbing materials for solar cell applications.* Journal of the American Chemical Society, 2015. **137**(24): p. 7843-7850.
38. Iagher, L. and L. Etgar, *Effect of Cs on the stability and photovoltaic performance of 2D/3D perovskite-based solar cells.* ACS Energy Letters, 2018. **3**(2): p. 366-372.

39. Li, N., et al., *Mixed cation FAxPEA1–xPbI3 with enhanced phase and ambient stability toward high-performance perovskite solar cells.* Advanced Energy Materials, 2017. **7**(1): p. 1601307.
40. Lee, J.-W., et al., *2D perovskite stabilized phase-pure formamidinium perovskite solar cells.* Nature communications, 2018. **9**(1): p. 3021.
41. Jiang, W., et al., *A new layered nano hybrid perovskite film with enhanced resistance to moisture-induced degradation.* Chemical Physics Letters, 2016. **658**: p. 71-75.
42. Soe, C.M.M., et al., *New type of 2D perovskites with alternating cations in the interlayer space,(C (NH2) 3)(CH3NH3) n Pb n I3 n+ 1: Structure, properties, and photovoltaic performance.* Journal of the American Chemical Society, 2017. **139**(45): p. 16297-16309.
43. Hojamberdiev, M., et al., *New Dion–Jacobson Phase Three-Layer Perovskite CsBa2Ta3O10 and Its Conversion to Nitrided Ba2Ta3O10 Nanosheets via a Nitridation–Protonation–Intercalation–Exfoliation Route for Water Splitting.* Crystal Growth & Design, 2016. **16**(4): p. 2302-2308.
44. Mao, L., et al., *Hybrid Dion–Jacobson 2D lead iodide perovskites.* Journal of the American Chemical Society, 2018. **140**(10): p. 3775-3783.
45. Li, X., et al., *Two-Dimensional Dion–Jacobson Hybrid Lead Iodide Perovskites with Aromatic Diammonium Cations.* Journal of the American Chemical Society, 2019. **141**(32): p. 12880-12890.
46. Liang, F., Z. Hui, and Y. Run-zhang, *Synthesis and characterization of a new triple-layered perovskite KSr 2 Nb 3 O 10 and its protonated compounds.* Journal of Wuhan University of Technology-Mater. Sci. Ed., 2002. **17**(2): p. 22-25.
47. Zhang, Y., et al., *Dynamical transformation of two-dimensional perovskites with alternating cations in the interlayer space for high-performance photovoltaics.* Journal of the American Chemical Society, 2019. **141**(6): p. 2684-2694.
48. Yun, Q., et al., *Layered Transition Metal Dichalcogenide-Based Nanomaterials for Electrochemical Energy Storage.* Advanced Materials, 2020. **32**(1): p. 1903826.
49. Tran, T.T., et al., *Quantum emission from hexagonal boron nitride monolayers.* Nature nanotechnology, 2016. **11**(1): p. 37-41.
50. Li, G., et al., *Architecture of graphdiyne nanoscale films.* Chemical Communications, 2010. **46**(19): p. 3256-3258.
51. Khan, K., et al., *Recent advances in two-dimensional materials and their nanocomposites in sustainable energy conversion applications.* Nanoscale, 2019. **11**(45): p. 21622-21678.
52. Zhou, J., et al., *2D space-confined synthesis of few-layer MoS2 anchored on carbon nanosheet for lithium-ion battery anode.* ACS nano, 2015. **9**(4): p. 3837-3848.
53. Cha, E., et al., *2D MoS 2 as an efficient protective layer for lithium metal anodes in high-performance Li–S batteries.* Nature nanotechnology, 2018. **13**(4): p. 337-344.
54. Wang, J., F. Ma, and M. Sun, *Graphene, hexagonal boron nitride, and their heterostructures: properties and applications.* RSC advances, 2017. **7**(27): p. 16801-16822.
55. Li, J., et al., *Metal-Free 2D/2D Black Phosphorus and Covalent Triazine Framework Heterostructure for CO2 Photoreduction.* ACS Sustainable Chemistry & Engineering, 2020. **8**(13): p. 5175-5183.
56. Lin, Y., et al., *Enhanced thermal stability in perovskite solar cells by assembling 2D/3D stacking structures.* The journal of physical chemistry letters, 2018. **9**(3): p. 654-658.

57. Chen, J., D. Lee, and N.-G. Park, *Stabilizing the Ag electrode and reducing J–V hysteresis through suppression of iodide migration in perovskite solar cells.* ACS applied materials & interfaces, 2017. **9**(41): p. 36338-36349.
58. Lee, D.S., et al., *Passivation of grain boundaries by phenethylammonium in formamidinium-methylammonium lead halide perovskite solar cells.* ACS Energy Letters, 2018. **3**(3): p. 647-654.
59. Koh, T.M., et al., *Enhancing moisture tolerance in efficient hybrid 3D/2D perovskite photovoltaics.* Journal of Materials Chemistry A, 2018. **6**(5): p. 2122-2128.
60. Wang, Z., et al., *Efficient ambient-air-stable solar cells with 2D–3D heterostructured butylammonium-caesium-formamidinium lead halide perovskites.* Nature Energy, 2017. **2**(9): p. 17135.
61. Yang, X., et al., *Efficient green light-emitting diodes based on quasi-two-dimensional composition and phase engineered perovskite with surface passivation.* Nature communications, 2018. **9**(1): p. 1-8.
62. Chu, Z., et al., *Large cation ethylammonium incorporated perovskite for efficient and spectra stable blue light-emitting diodes.* Nature communications, 2020. **11**(1): p. 1-8.
63. Mao, L., et al., *Role of organic counterion in lead-and tin-based two-dimensional semiconducting iodide perovskites and application in planar solar cells.* Chemistry of Materials, 2016. **28**(21): p. 7781-7792.
64. Cao, D.H., et al., *Thin films and solar cells based on semiconducting two-dimensional ruddlesden–popper (CH3 (CH2) 3NH3) 2 (CH3NH3) n− 1Sn n I3 n+ 1 perovskites.* ACS Energy Letters, 2017. **2**(5): p. 982-990.
65. Protesescu, L., et al., *Nanocrystals of cesium lead halide perovskites (CsPbX3, X= Cl, Br, and I): novel optoelectronic materials showing bright emission with wide color gamut.* Nano letters, 2015. **15**(6): p. 3692-3696.
66. Lian, L., et al., *Colloidal synthesis of lead-free all-inorganic cesium bismuth bromide perovskite nanoplatelets.* CrystEngComm, 2018. **20**(46): p. 7473-7478.
67. Mitzi, D.B., et al., *Conducting tin halides with a layered organic-based perovskite structure.* Nature, 1994. **369**(6480): p. 467.
68. Chen, M., et al., *Lead-Free Dion–Jacobson Tin Halide Perovskites for Photovoltaics.* ACS Energy Letters, 2018. **4**(1): p. 276-277.
69. Tsai, H., et al., *High-efficiency two-dimensional Ruddlesden–Popper perovskite solar cells.* Nature, 2016. **536**(7616): p. 312.
70. Chen, Y., et al., *Tailoring Organic Cation of 2D Air-Stable Organometal Halide Perovskites for Highly Efficient Planar Solar Cells.* Advanced Energy Materials, 2017. **7**(18): p. 1700162.
71. Zhang, X., et al., *Vertically oriented 2D layered perovskite solar cells with enhanced efficiency and good stability.* Small, 2017. **13**(33): p. 1700611.
72. Smith, M.D., et al., *Decreasing the electronic confinement in layered perovskites through intercalation.* Chemical science, 2017. **8**(3): p. 1960-1968.
73. Yang, J., et al., *Investigation of CH3NH3PbI3 degradation rates and mechanisms in controlled humidity environments using in situ techniques.* ACS nano, 2015. **9**(2): p. 1955-1963.
74. Safdari, M., et al., *Layered 2D alkyldiammonium lead iodide perovskites: synthesis, characterization, and use in solar cells.* Journal of Materials Chemistry A, 2016. **4**(40): p. 15638-15646.
75. Safdari, M., et al., *Structure and function relationships in alkylammonium lead (ii) iodide solar cells.* Journal of Materials Chemistry A, 2015. **3**(17): p. 9201-9207.
76. Zuo, L., et al., *Polymer-modified halide perovskite films for efficient and stable planar heterojunction solar cells.* Science advances, 2017. **3**(8): p. e1700106.

77. Yao, K., et al., *Multilayered perovskite materials based on polymeric-ammonium cations for stable large-area solar cell.* Chemistry of Materials, 2016. **28**(9): p. 3131-3138.
78. Misra, R.K., et al., *Temperature-and component-dependent degradation of perovskite photovoltaic materials under concentrated sunlight.* The journal of physical chemistry letters, 2015. **6**(3): p. 326-330.
79. Pollard, R.T., et al., *Southern Ocean deep-water carbon export enhanced by natural iron fertilization.* Nature, 2009. **457**(7229): p. 577-580.
80. Yang, S.H., et al., *Tris (thiocyanate) Ruthenium (II) Sensitizers with Functionalized Dicarboxyterpyridine for Dye-Sensitized Solar Cells.* Angewandte Chemie, 2011. **123**(36): p. 8420-8424.
81. Frost, J.M., et al., *Atomistic origins of high-performance in hybrid halide perovskite solar cells.* Nano letters, 2014. **14**(5): p. 2584-2590.
82. Wehrenfennig, C., et al., *High charge carrier mobilities and lifetimes in organolead trihalide perovskites.* Advanced materials, 2014. **26**(10): p. 1584-1589.
83. Milot, R.L., et al., *Charge-carrier dynamics in 2D hybrid metal–halide perovskites.* Nano letters, 2016. **16**(11): p. 7001-7007.
84. Xu, R.-P., et al., *In situ observation of light illumination-induced degradation in organometal mixed-halide perovskite films.* ACS applied materials & interfaces, 2018. **10**(7): p. 6737-6746.
85. Pedesseau, L., et al., *Advances and promises of layered halide hybrid perovskite semiconductors.* ACS nano, 2016. **10**(11): p. 9776-9786.
86. Chen, A.Z., et al., *Origin of vertical orientation in two-dimensional metal halide perovskites and its effect on photovoltaic performance.* Nature communications, 2018. **9**(1): p. 1336.
87. Tsai, H., et al., *Design principles for electronic charge transport in solution-processed vertically stacked 2D perovskite quantum wells.* Nature communications, 2018. **9**(1): p. 2130.

Chapter 3

3 Experimental

3.1 Introduction

The synthesis of $CsPbBr_3$ thin films on FTO substrate by a two-step solution method that included spin coating followed by dip coating is reported. A quasi-2D perovskite ($PEA_2Cs_{n-1}Pb_nBr_{3n+1}$) is also prepared by spin-coating a solution of isopropanol containing PEABr onto as-prepared $CsPbBr_3$ to facilitate the partial removal of the A-cation (Cs^+) by an organic spacer (PEA^+). An overview of the fabrication of $CsMAFAPb(IBr)_3$ and $CsPbBr_3$-based solar cells is provided. The various characterization methods used in this study, including XRD, SEM, Raman, and I-V measurements, are described.

3.2 Synthesis of $CsPbBr_3$ and $CsPbBr_3$/PEABr HaP thin film

3.2.1 Chemicals

Cesium bromide (99.99%), Lead bromide (99.99%), Acetone, methanol, Isopropanol, Ethanol, Phenethylammonium bromide, Dimethylformamidinium (DMF), spiro-OMeTAD, titanium isopropoxide, (trifluoromethane)sulfonimide lithium salt (LiTFSI), and tris(2-(1Hpyrazol-1-yl)-4-tert-butylpyridine)cobalt(III)tri[bis-(trifluoromethane)sulfonimide] (FK209), and acetonitrile were all purchased from sigma aldrich South Africa..

3.2.2 Substrate preparation

Figure 3-1 shows how the substrates were cleaned. The ITO substrates were cleaned using sequential sonication in acetone, isopropanol, and deionized water for 30 min, followed by drying under pressurized nitrogen.

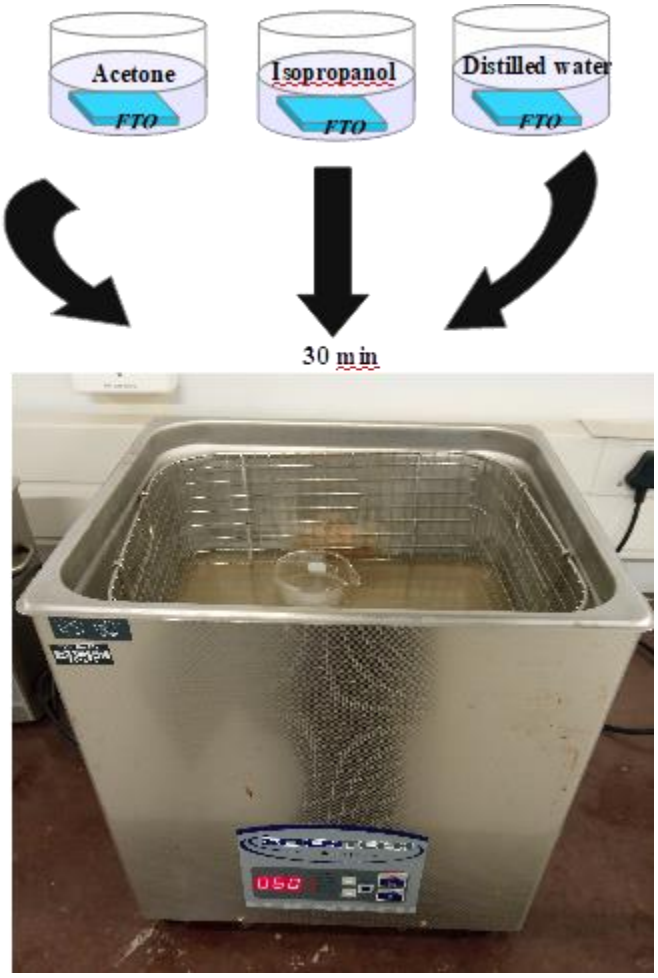

Figure 3-1: Cleaning of substrates by sonication.

3.2.3 Preparation of $CsPbBr_3$ and thin film

To prepare the $CsPbBr_3$ HaP precursor solutions, 30 mg of CsBr was dissolved in 2 mL of methanol and heated for 10 min in a sealed container. After that, 367 mg of $PbBr_2$ were dissolved in 1 mL of DMF, which was stirred at 75 °C on a hot plate for one hour, and then a 0.22 µm pore PTFE filter was used immediately for filtration. $CsPbBr_3$ thin films were synthesized by spin-coating a layer of $PbBr_2$ at 4000 rpm for 40 s on the preheated (75 ℃) FTO substrate and dried at 75 ℃ for 30 min. The substrates were then dipped for 15 min in a preheated (50 ℃) solution of 15 mg/mL CsBr and then annealed at 180 ℃ immediately on a hot plate for 30 min.

3.2.4 Preparation of $CsPbBr_3$/PEABr HaP film

Different mass percents of PEABr were dissolved in 1 mL of isopropanol solutions according to Equation 1,

$$\frac{Mass_{PEABr}}{Vol_{Isopropanol}} = \%x \qquad \text{Equation 1}$$

where $Mass_{PEABr}$ is the mass of PEABr, $Vol_{Isopropanol}$ is the volume of isopropanol and $\%x$ is the molar concentration of PEABr [1]. The PEABr/isopropanol solution was placed on a hot plate at 50 °C for 3 min to dissolve PEABr. In order to synthesise a 2D HaP of the form $PEA_2Cs_{n-1}Pb_nBr_{3n+1}$ thin film, the different molar weights of PEABr dissolved in isopropanol were then spin-coated at 5000 rpm for 30 s on the as-prepared $CsPbBr_3$ thin films and annealed at 110 °C for 20 min (Figure 3-2)

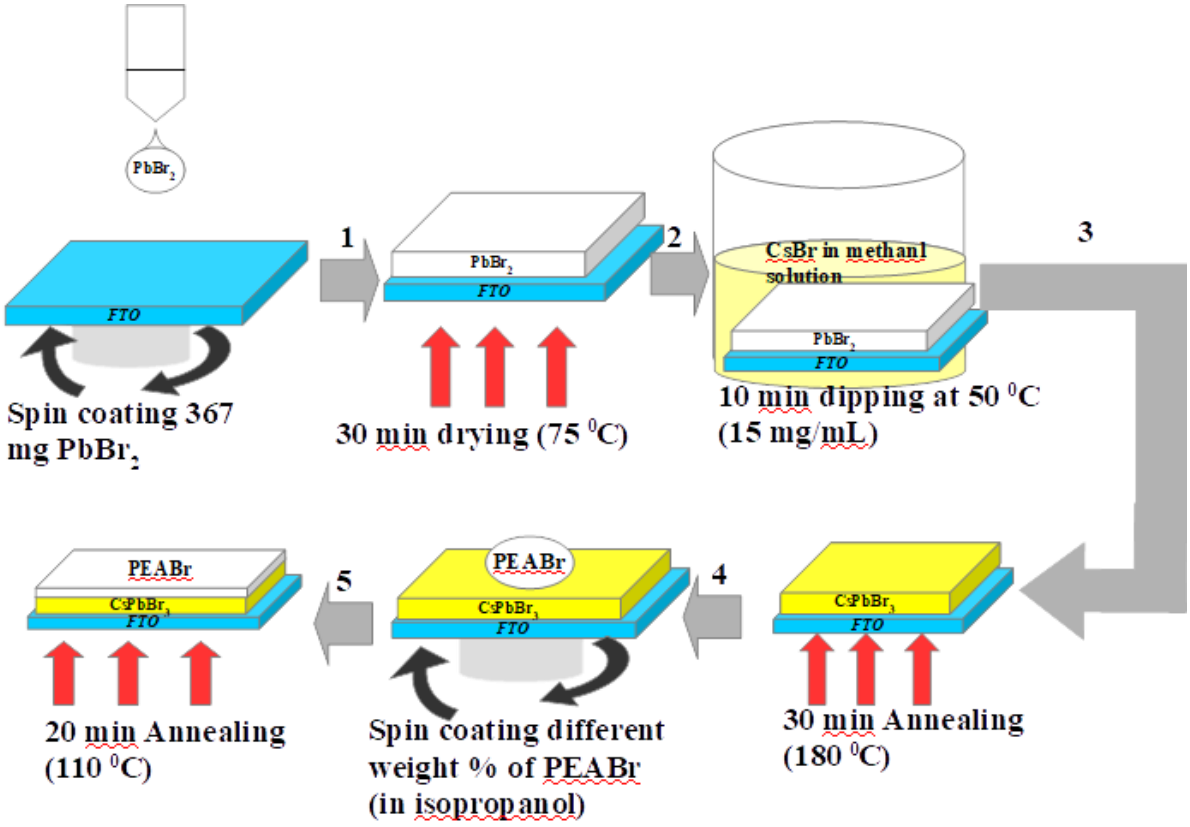

Figure 3-2: Synthesis of $CsPbBr_3$/PEABr

3.3 $CsPbBr_3$ device fabrication

3.3.1 Preparation of TiO_2 layer

Figure 3-3 shows the schematic representation of titanium dioxide (TiO_2) deposition by spray pyrolysis using the artist spray gun. Following the substrate cleaning process, the electron transport layer (ETL) was synthesized by spray pyrolysis. To prepare TiO_2 precursor, 0.5 M titanium isopropoxide was prepared in butanol. This solution was then sprayed onto the ITO substrate and then the samples were placed in a furnace and heat treated at 500 ℃ to form a compact TiO_2 layer. During the deposition process, the substrate temperature was set to 250 ℃ (a low deposition temperature would affect the evaporation of the solvents [2] on the hot plate) and the distance between the substrate and the spray gun nozzle was set to 15 cm as shown in *Figure 3-3*. The TiO_2 precursor was sprayed on the substrate for 30 s followed by a 1 min pause for 3 cycles.

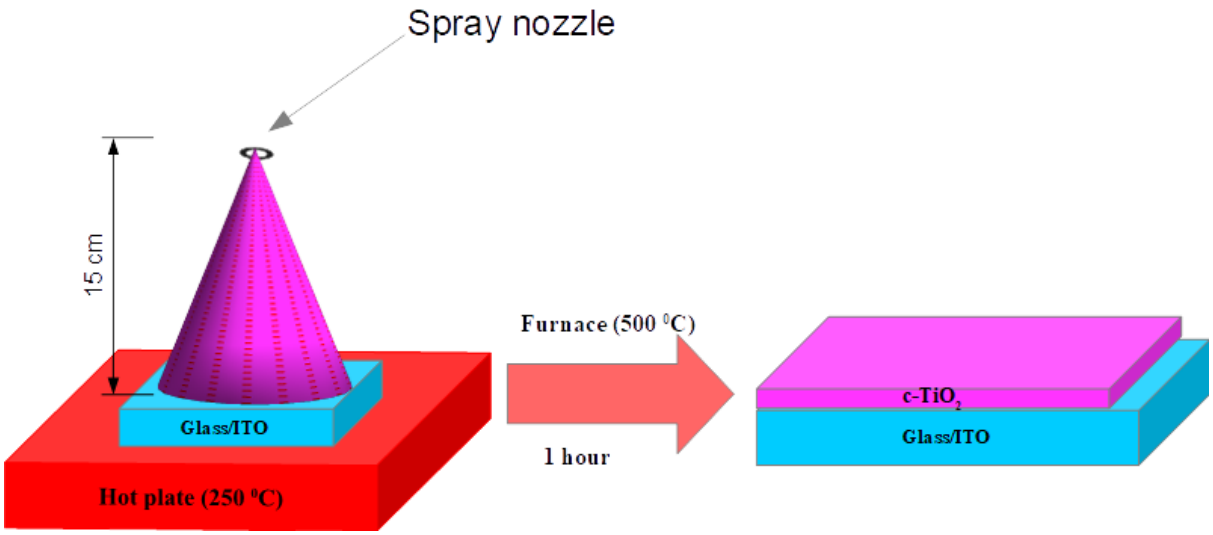

Figure 3-3: Schematic representation of TiO_2 deposition by spray pyrolysis.

3.3.2 Synthesis of Spiro-OMeTAD HTL and deposition of electrodes.

To complete the HaP solar cell device with the architecture shown in *Figure 3-4*, a Spiro-OMeTAD solution was spin-coated on the annealed $CsPbBr_3$ film at 3000 rpm for 30 s as a HTL. The spiro-OMeTAD was synthesized by preparing stock solutions of (trifluoromethane)sulfonimide lithium salt (LiTFSI), and tris(2-(1Hpyrazol-1-y l) - 4 - t e r t-butylpyridine)coba l t (I I I) t r i [b i s - (trifluoromethane)sulfonimide] (FK209), in

acetonitrile. Firstly, 2 mL of spiro-OMeTAD chlorobenzene solution (80 mg mL^{-1}) was prepared and stirred for a few min at room temperature, then, 57,6 µL 4-tertbutylpyridine, 35 µL LiTFSI acetonile solution (520 mg mL^{-1}), and 35 µL FK209 acetonitrile solution (300 mg mL^{-1}) were added in this order. The spiro-OMeTAD (50 µL) was deposited by dropping the solution in the middle of the ITO substrate and spin-coated at 4000 rpm for 30 s. In the last 10 s, chlorobenzene was rapidly dropped in the middle of the substrate. The spiro-OMeTAD should look homogeneously distributed and smooth on top of the HaP. LiTFSI is highly hygroscopic, and can, therefore, produce visible aggregates. This could indicate that the additives were not fully dissolved or hydrated. An excess of LiTFSI results in a drop in the open circuit voltage (V_{oc}) [3]. Finally, an 80 nm thick Ag layer was deposited by thermal evaporation at a pressure of 5×10^{-6} mbar and a rate of 0.2 Å/s.

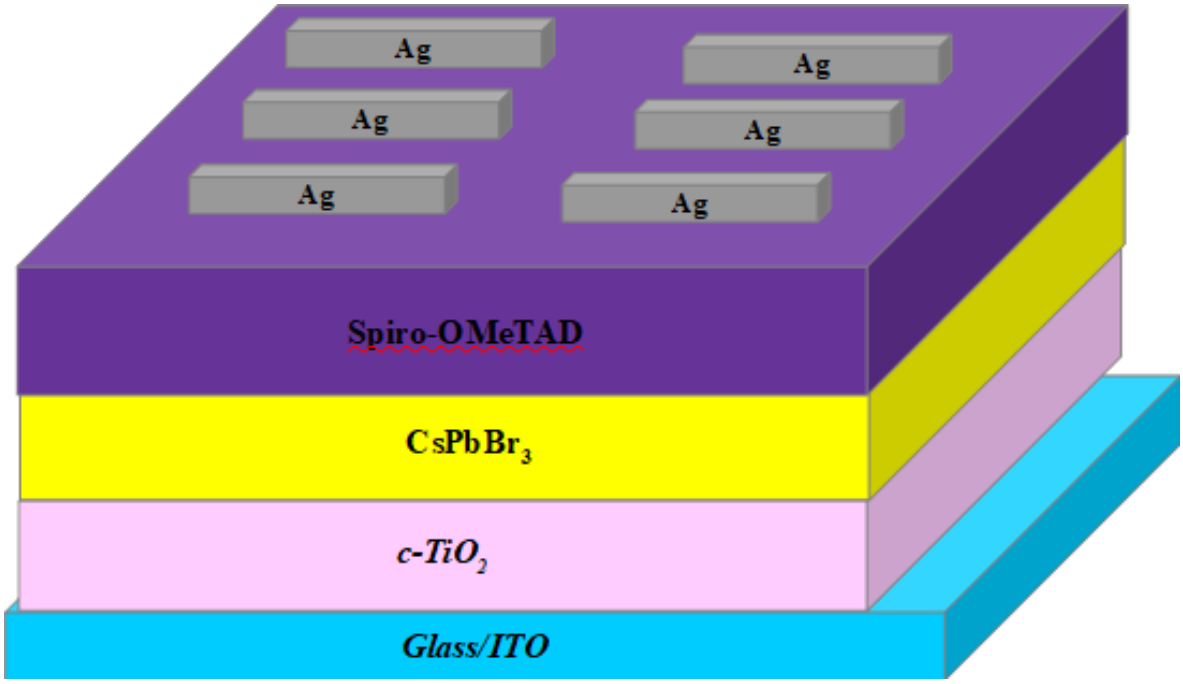

Figure 3-4: Architecture of pristine solar cell.

3.4 Material characterization

All the measurements for the $CsPbBr_3$/PEABr HaP were carried out in ambient air and at room temperature without encapsulation.

3.4.1 X-ray diffraction (XRD)

X-ray diffraction analysis is a technique that is used to determine the crystallographic structure of a material in materials science. It is a non-distractive technique that identifies

crystalline phases and orientation, as well as structural properties such as lattice parameters, strain, grain size, phase composition, and preferred orientation. This information can be used to determine how the actual structure of a material deviates from the ideal one [4].

Cu and Co anode with the specific wavelengths of λ = 1.789 Å and λ = 1.5406, respectively, are the most commonly used anode materials [1]. The crystal atoms scatter incident X-rays primarily by interacting with the electrons in the atoms. A regular array of electrons produces a regular array of spherical waves. In most directions, these waves cancel each other out through destructive interference, but in certain directions, they are added constructively as determined by Bragg's law [5]:

$$2dsin\,\theta = n\lambda \qquad \textit{Equation 2}$$

Where d is the spacing between diffraction planes, θ is the incident angle, n is an integer, and λ is the beam wavelength. A set of d-spacing values for a typical XRD scan can provide the characteristic features of a sample which is investigated. The crystal structure of the material is then determined from the known d-spacing values of the crystallographic planes of the samples. To calculate the lattice parameters of a simple tetragonal crystal, where $= b \neq c$, the following equation can be used [5]:

$$\frac{1}{(d_{hkl})^2} = \frac{h^2}{a^2} + \frac{k^2}{b^2} + \frac{l^2}{c^2} \qquad \textit{Equation 3}$$

Where h, k, l are Miller indices, and a, b, and c are the lattice parameters. The Miller indices indicate the orientation of a plane or a set of parallel planes of atoms in a crystal. The crystallite size can also be calculated from the XRD data using the equation:

$$D = \frac{0.9\lambda}{\beta_{hkl}\cos\theta} \qquad \textit{Equation 4}$$

Where D is the average crystallite size, λ is the wavelength of the X-rays, β is the full width at half maximum, and θ is the Braggs angle. The Bruker D2-Phaser X-ray diffractometer that contains Cu Kα radiation with a wavelength of 0.154 nm was used to determine the structural

properties of $CsPbBr_3$ and $CsPbBr_3$/PEABr. The angle between the incident and diffracted rays, 2θ was varied from 10° to 50° in steps of 0.05. *Figure* 3-5 shows a schematic representation of the XRD layout.

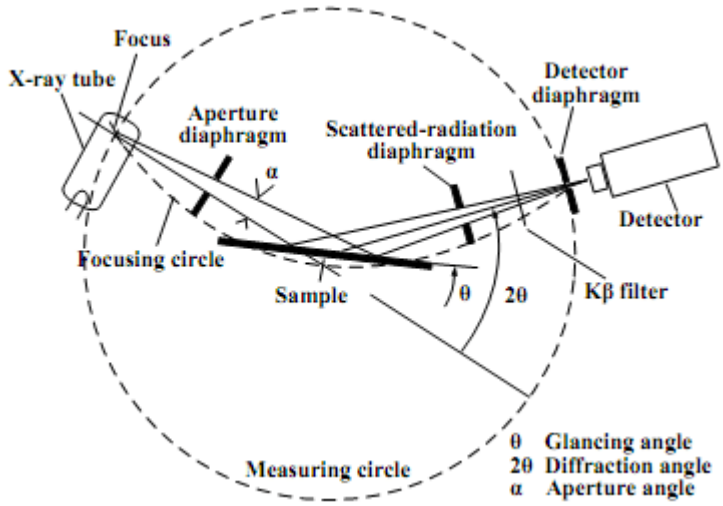

Figure 3-5: XRD schematic layout [6].

3.4.2 Scanning electron microscopy (SEM)

Scanning electron microscopy (SEM) is one of the common methods for imaging the microstructure and morphology of materials at the macroscale or nanoscale. In SEM, a low-energy electron beam illuminates and scans the surface of the sample. The electron beam is accelerated by a high voltage of ~ 40 kV, which is narrowed after passing the aperture and the electromagnetic lens to 1 kV or less. As the beam reaches the material, some distinct interactions occur, emitting photons and electrons from or near the sample surface [7]. The received signal generated by the electron-sample interaction to generate an image is detected by the different types of detectors, depending on the SEM mode that is used. There are various SEM modes, such as X-ray mapping, secondary electron imaging, backscattered electron imaging, electron channeling, and Auger electron microscopy, for the characterization of materials (including biomaterials [7]. The secondary electrons are responsible for imaging to obtain the morphology of the sample. In this study, the $CsPbBr_3$ and $CsPbBr_3$/PEABr surface morphologies were characterized with the field emission scanning electron microscopy (FE-SEM ZEISS SEM-Microscope Crossbeam-540) acquired by an in-lens detector operating at an accelerating voltage of 2.0 kV. Carbon coating of the samples was performed before the

samples were loaded into the chamber. *Figure* 3-6 shows a schematic representation of the SEM instrument.

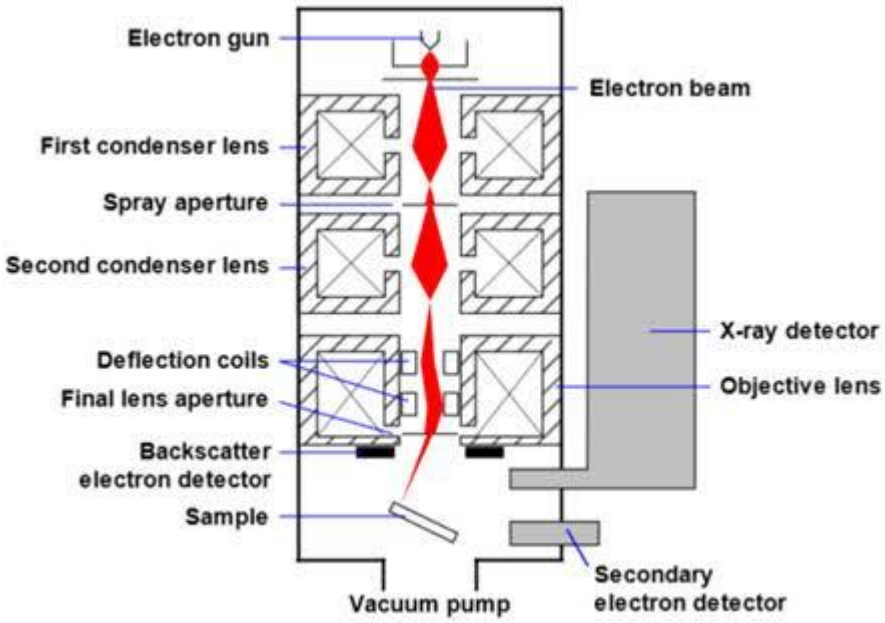

Figure 3-6: Schematic representation of SEM [8].

3.4.3 Ultraviolet-visible (UV-vis) spectroscopy

Figure 3-7 shows how the light travels through the UV-vis spectrometer. A UV-vis spectrometer measures light absorbance across the ultraviolet and visible ranges of the electromagnetic spectrum to understand how radiation interacts with the sample. Incident light can either be absorbed, reflected, or transmitted when it strikes matter. Atomic excitation is caused by the absorbance of radiation in the UV-vis range, which changes molecules from the low-energy ground state to an excited state. Before the atom can changes its excitation state, it must absorb enough radiation to allow for an electron to move into higher molecular orbits. A UV-vis absorption can be determined by comparing the intensity of light passing through (I) to the initial intensity (I_o).

Varian Cary 60 UV-Vis Spectrometer was used to study the optical absorbance of $CsPbBr_3$ and $CsPbBr_3$/PEABr thin films. The absorbance measurements were done in the wavelength range of 200-800 nm. Before measuring the absorbance of the $CsPbBr_3$ film, a baseline correction was done (to separate the true spectroscopic signals from interference effects from the FTO substrate) by placing a clean FTO substrate with the coated side facing

the light source. Subsequently, the $CsPbBr_3$ was placed on the sample holder in the UV-vis spectrometer and characterised to observe the absorbance of the sample. This entire procedure was repeated to find the absorption spectrum of the $CsPbBr_3$/PEABr samples.

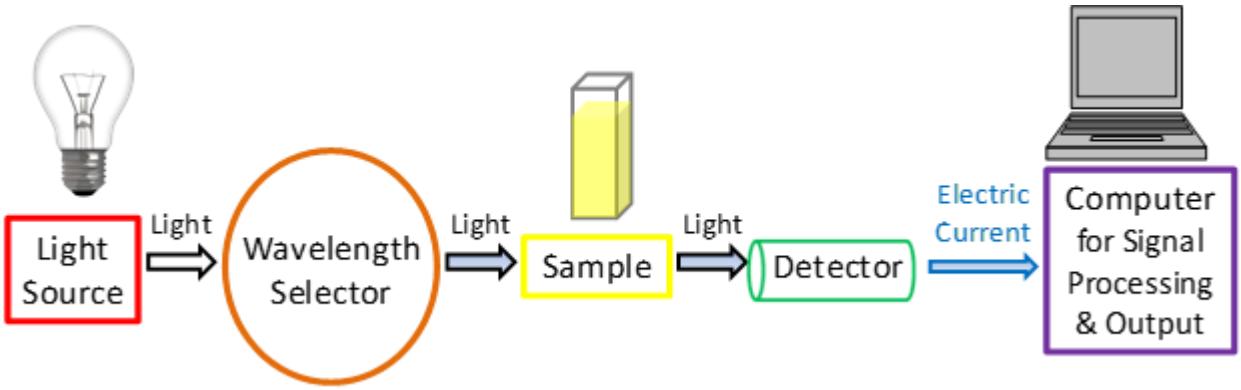

Figure 3-7: Schematic operation of the UV-vis spectrometer.

3.5 Synthesis of $CsMAFAPb(IBr)_3$ thin film

3.5.1 Substrate preparation

FTO substrates were brushed using a soft cloth to remove dust particles without causing damage to the surface. This was followed by rinsing with deionized water, and a 15 min ultrasonic bath in a 2% Hellmanex solution. After removing the substrates from the solution, they were rinsed thoroughly with deionized water. A Decon acid rinse solution was used to further decontaminate the substrates. The process is completed by rinsing in lots of deionized water. Subsequently, the substrates were sonicated in a preheated (70 °C) solution of decon90 for 15 min and then rinsed with plenty of deionized water. Next, the substrates were dried with nitrogen flow under pressure. Plasma cleaning with argon gas was performed on the substrates to remove some residuals from the surface of the substrates for 15 min. The substrates were then immediately used to avoid streaks and spots on the surface.

3.5.2 Preparation of $CsMAFAPb(IBr)_3$ precursor

The $CsMAFAPb(IBr)_3$ was synthesized by preparing stock solutions of 1.5 mol of PbI_2 and $PbBr_2$ per litter of 4:1 V/V dimethylformamide (DMF)/dimethyl sulfoxide (DMSO). The stock solution was heated to 180 °C for 10 min and then stored for a long time, and reheated to 180 °C before use. By weighing out 1 g of formamidinium iodide (FAI) and 1 g of

methylammonium bromide (MABr) powders in separate vials, a ratio of 1:1:0.9 (that is, 9% excess lead) was obtained. Following this, 1.5 mol/L of PbI2(PbBr2) was added to the vials containing FAI(MABr) powder. A clear solution was achieved after shaking the solution for a few minutes. The intermediate precursor solution of the form $(FAPbI_3)_{83}(MAPbBr_3)_{17}$ is prepared by mixing a 5:1 V/V ratio of $FAPbI_3$ and $MAPbBr_3$ (with excess PbI_2). The CsI stock solution was prepared by dissolving 1.5 mol of CsI in DMSO. The solution was heated at 150 ℃ with staring until the solution looks clear. The CsI stack solution was also stored for a long time. It was not necessary to rewarm it before use. The $CsMAFAPb(IBr)_3$ precursor solution is prepared by mixing 5 vol % of CsI stock solution in the intermediate HaP solution.

3.6 $CsMAFAPb(IBr)_3$ device fabrication

As soon as the substrates were cleaned with plasma, they were transferred to a hot plate and warmed to 450 °C. The substrates were subsequently sprayed with a solution of TiO_2 to form a compact TiO_2 layer by aerosol spray pyrolysis. The TiO_2 solution contained 0.4 mL of acetylacetone and 0.6 mL of titanium diisopropoxide bis(acetylacetonate) in 9 mL of ethanol. Acetylacetone was added to ethanol, followed by the addition of diisopropoxide bis(acetylacetonate). Oxygen gas was used as a carrier gas for the TiO_2 solution. The spray gun nozzle was approximately 20 cm from the FTO substrate and at an angle of 45^o. The nozzle was moved around in a circular motion for 1 min with 20 s delay between each circle. The samples were then left in the hot plate for 10 min before cooling down whilst on the hot plate. Plasma cleaning with oxygen gas was done before the samples are quickly placed in the glove box to avoid wetting of the TiO_2.

The $CsMAFAPb(IBr)_3$ HaP film is deposited by a two-step method. First, a slow step at 1000 rpm and 200 rpm/s for 10 s to facilitate a full surface coverage after the solution is dropped in the middle of the substrate and a subsequently fast step at 6 000 rpm and 2 000 rpm/s for 20 s. In the second step, 200 µL of the antisolvent (chlorobenzene) is rapidly dropped in the middle of a 2 x 2 cm^2 substrate. Manual practice is required to acquire the right pressure induced by hand because dropping the antisolvent is one of the most delicate. Dropping the antisolvent too fast results in the HaP precursor being washed off and a whole forms in the centre. Whilst, dropping the antisolvent too slowly can induce cracks in the final film. The substrates are then immediately placed on a hot plate (100 ℃ for 1 hour) after spin-coating the antisolvent. A semitransparent, brown-like-coloured HaP film should appear before annealing, whereas, the samples turn opaque black *(Figure 3-8)* in a few minutes on a hot plate. Inhomogeneity,

pinholes, and cracks in the film surface can affect the device's performance. The samples are left to cool to room temperature in the glove box.

Figure 3-8: HaP film post-annealing.

Following the HaP film deposition, the spiro-OMeTAD was prepared and deposited by dropping the solution in the middle of a 2 x 2 cm^2 FTO substrate as described above. Prior to gold deposition, the samples are stored in a dark environment and with dry air to allow the lithium doping of the spiro-OMeTAD to occur. The gold layer *(Figure 3-9(a))* is deposited at a pressure of 5.0×10^{-6} mbar and at a rate of 1.2 Å/s up to 100 nm thickness. Two opposite ends of the sample were wiped with DMF to remove the spiro-OMeTAD and HaP film. A soldering wire was then used to contact the gold *(Figure 3-9 (b))*.

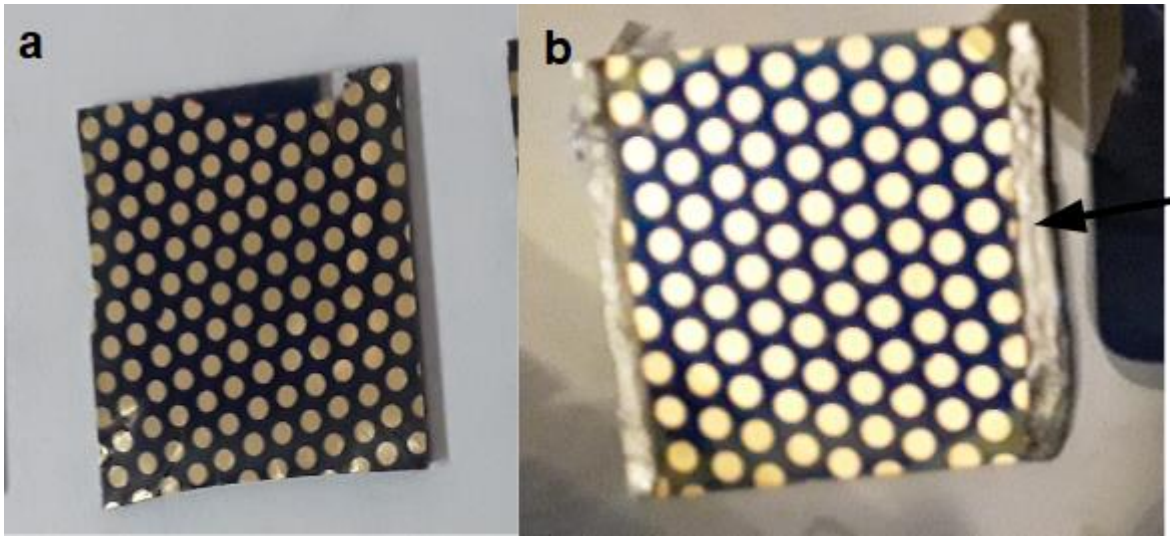

Figure 3-9: HaP solar cell (a) without a soldering wire (b) with soldering wire.

3.7 Device characterization of $CsMAFAPbBr_3$ –based solar cells

The electrical measurements of the $CsMAFAPbBr_3$ were done in a nitrogen-filled glovebox and, before testing, the devices are left resting overnight in the dark and dry air (below 1% relative humidity). The J-V curve of the 2 x 2 cm^2 substrates was obtained in a 2-wire source sense configuration using the Keithley 2400. The lighting used was an Oriel-class AAA xenon lamp-based solar simulator, providing approximately 100 mW / cm AM1.5G irradiance, while monitoring intensity with Si photodiodes.

3.8 REFERENCES

1. Leng, Y., *Materials characterization: introduction to microscopic and spectroscopic methods*. 2009: John Wiley & Sons.
2. Abd Hamed, N.K., N.A. Adam, and M.K. bin Ahmad. *Effects of Annealing Temperature of TiO2 Thin Film Deposited by Spray Pyrolysis Deposition Method for Dye-Sensitized Solar Cell (DSSC) Application*. in *Applied Mechanics and Materials*. 2015. Trans Tech Publ.
3. Abate, A., et al., *Lithium salts as "redox active" p-type dopants for organic semiconductors and their impact in solid-state dye-sensitized solar cells.* Physical Chemistry Chemical Physics, 2013. **15**(7): p. 2572-2579.
4. Whittig, L. and W. Allardice, *X-ray diffraction techniques.* Methods of Soil Analysis: Part 1 Physical and Mineralogical Methods, 1986. **5**: p. 331-362.
5. Bond, W.L., *Precision lattice constant determination.* Acta Crystallographica, 1960. **13**(10): p. 814-818.
6. Termtanun, M., *Photocatalytic degradation of pesticides using TiO2 nanoparticles*. 2013, University of Nottingham.
7. Kumar, S.S., et al., *Structure, morphology, and optical properties of amorphous and nanocrystalline gallium oxide thin films.* The Journal of Physical Chemistry C, 2013. **117**(8): p. 4194-4200.
8. Haque, M. and M. Saif, *In-situ tensile testing of nano-scale specimens in SEM and TEM.* Experimental mechanics, 2002. **42**(1): p. 123-128.

Chapter 4

4 Results and discussions

4.1 Introduction

The morphology, optical and structural properties of cesium lead bromide ($CsPbBr_3$) are discussed in this section. This chapter also presents the effects of phenethylammonium bromide (PEABr) mass percent on the $CsPbBr_3$ thin films. An analysis of current-voltage characteristics is presented for a solar cell containing an absorber layer of $CsPbBr_3$. Also discussed are the time-resolved photoluminescence (TRPL) and I-V measurements of the solar cell device with an absorbing layer of $CsMAFAPb(IBr)_3$.

4.2 Synthesis and characterization of $CsPbBr_3$

4.2.1 Morphology

Figure 4-1 shows a micrograph of $CsPbBr_3$ with its surface morphology characterized by scanning electron microscopy (SEM). The morphology exhibits some isolated cuboidal grains as well as a discontinuous surface with pinholes. The average grain size was found to be 433 nm. Yang *et al*. reported on the synthesis of $CsPbBr_3$ thin film with a different additive to improve the photoelectric performance of the device. Their pristine $CsPbBr_3$ thin film attained an average grain size of 410 nm with poor surface coverage [1]. The growth of larger grains in $CsPbBr_3$ films is at the expense of smaller $CsPbBr_3$ grains due to their reduced surface energy [2]. According to Zhang *et al*. the performance of the overall cell is dependent on the average grain size, amongst other properties. Perovskite films with a large average grain size have been proven to contain high carrier mobilities [3]. Poor surface coverage occurs when pinholes form in the final layer when using a two-step solution preparation process [4]. These pinholes can be observed from the SEM images in *Figure 4-1*.

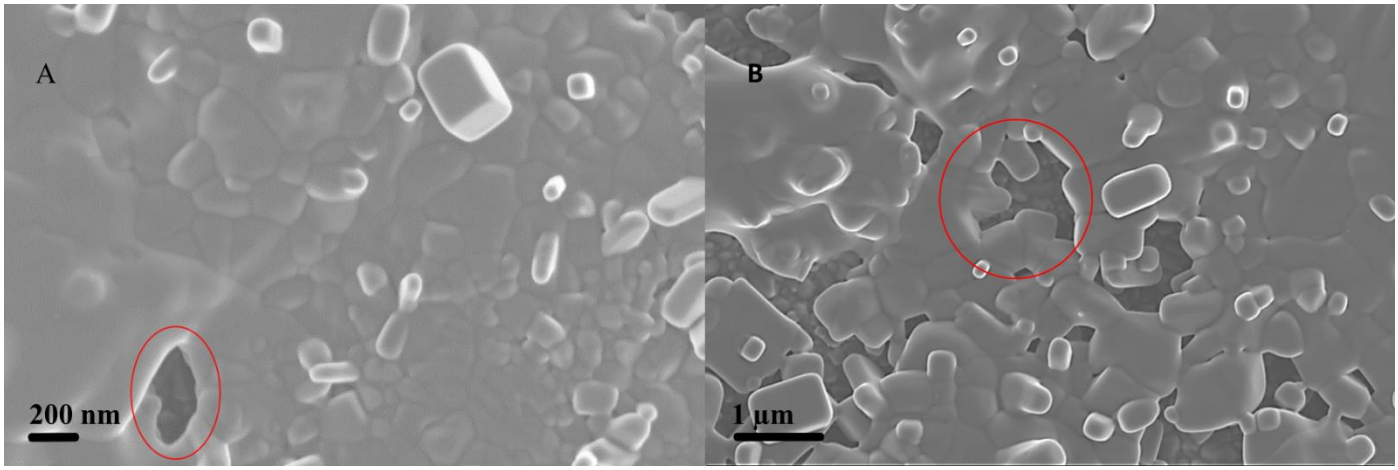

Figure 4-1: Morphology of $CsPbBr_3$ thin film.

4.2.2 Optical properties

Figure 4-2 shows the optical study performed on the $CsPbBr_3$ film, using UV-vis spectroscopy to evaluate the absorption spectra and bandgap. The absorption spectrum shows an onset at 533 nm and an excitonic peak at 518 nm, which are of $CsPbBr_3$ thin films. Tauc plots indicate that a bandgap of 2.3 eV is known for $CsPbBr_3$ thin films. The results are consistent with those obtained by Nasi *et al*. in their investigation of an alternative technique for the deposition of $CsPbBr_3$ thin films that are highly stable and pinhole-free [5]. Their films had a bandgap of 2,3 eV, with an absorption onset at 530 nm and an excitonic peak at 515 nm.

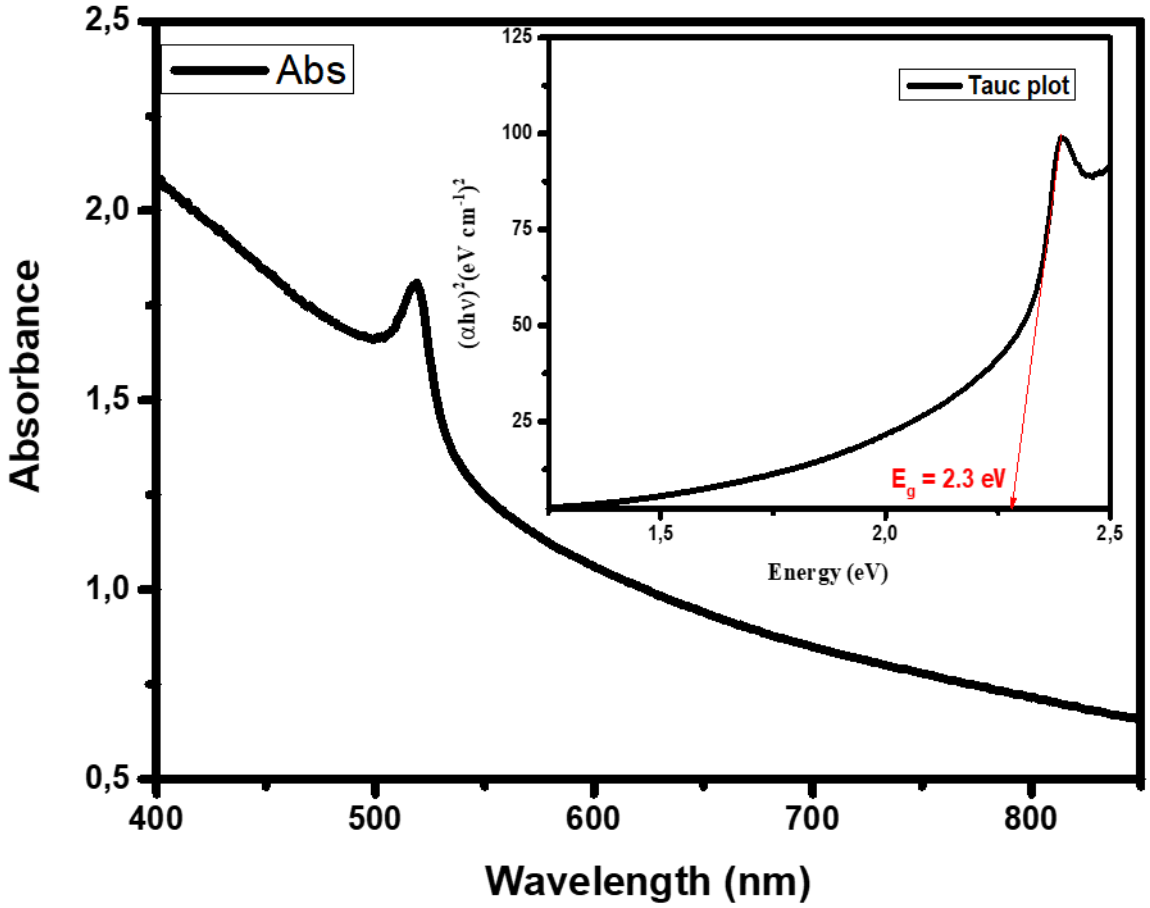

Figure 4-2: Absorbance spectra and Tauc plot of $CsPbBr_3$ thin film.

4.2.3 Structural properties

The phase purity and crystallinity of the $CsPbBr_3$ were examined with X-ray diffraction (XRD), and the diffraction patterns are shown in *Figure 4-3*. $CsPbBr_3$ has measured peaks at 15.38°, 21.78°, 26.59°, 30.81°, 33.71°, and 37.87°, which correspond respectively to the (100), (110), (111), (200), (210) and (211) diffraction planes [6]. The crystal structure of $CsPbBr_3$ is cubic with space group *Pm-3m* and lattice parameters $a = b = c = 5.830$ Å. These values match exactly with the standard data (JCPDS Card No 00-054-0752). However, the two-step solution-based methods for synthesizing $CsPbBr_3$ are accompanied by impurity phases of $CsPb_2Br_5$ and/or Cs_4PbBr_6, which limit the efficiency of $CsPbBr_3$-based devices [7]. Additional peaks appear at 11.78°, 18.88°, 23.45°, 29.49°, and 35.48°, respectively.

According to Liu et al, these peaks can be attributed to the tetragonal $CsPb_2Br_5$ (denoted by *) structure which vanishes during the annealing step.

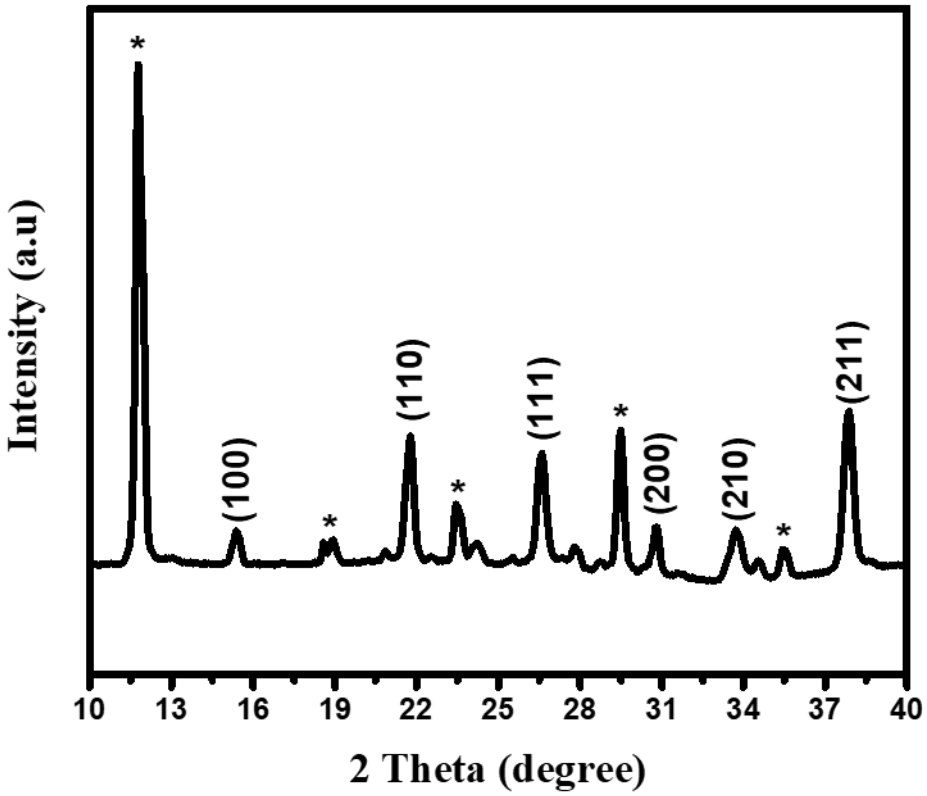

Figure 4-3: X-ray diffraction pattern of $CsPbBr_3$ film deposited on FTO substrate

The broadening of the X-ray line, which is measured from the full width at half maximum, is one of the distinguishing characteristics of the XRD signature. The instrumental effect, crystallite size effect, and micro-strain are the causes of it. One of the distinguishing traits of XRD signatures, X-ray line broadening is calculated from the full width half maximum (FWHM) of the diffraction peaks. Essentially, it is caused by three things: microstrains, the size of the crystallites, and instrumental effects [8]. An FWHM of 0.3168° was calculated from the XRD peaks of $CsPbBr_3$ using the Gaussian fit. This value was then used to calculate the crystallite size (25.07 nm) by utilizing the Scherrer equation:

$$D = \frac{k\lambda}{\beta \cos \theta} \qquad \textit{Equation 5}$$

where D is the crystallite size (nm), k is constant (0.9), λ is the wavelength of the incident X-ray (~0.154 nm), β is the FWHM (radians) and θ is the diffraction Bragg angle ($\frac{2\theta}{2}$).

4.2.4 $CsPbBr_3$ solar cell device

HaP thin films with a large average grain size have high carrier mobilities, however, the presence of pinholes can provide direct contact between the electron transport layer (ETL) and hole transport layer (HTL) [9], thereby limiting the charge extraction efficiency. These pinholes act as trap-assisted recombination centers for electrons and holes [10]. Further, they can introduce surface defects into the device structure, reducing photocurrent and voltage, and ultimately affecting the performance of the cell [11]. *Figure 4-4* shows a graph of Current-Voltage (J-V) properties of the as-prepared $CsPbBr_3$ PSC with a low fill factor (FF) of 30.89%. The low FF can be attributed to the loss of charge carriers occurring at the site where there are pinholes, which ultimately reduce the PCE of the solar cell.

A low V_{oc} of 0.3 eV was achieved from the $CsPbBr_3$ solar cell device and can be a result of the shunt resistance which is known to reduce the open-circuit voltage (V_{oc}) as well as the FF for solar cells [12]. Incomplete perovskite film coverage leads to shunt pathways accompanied by the internal charge carrier recombination, which affects the power conversion efficiency (PCE). PCE is strongly affected by film coverage, pinhole density, and grain size [12]. It is possible that these factors accounted for the low PCE of 0.96 %.

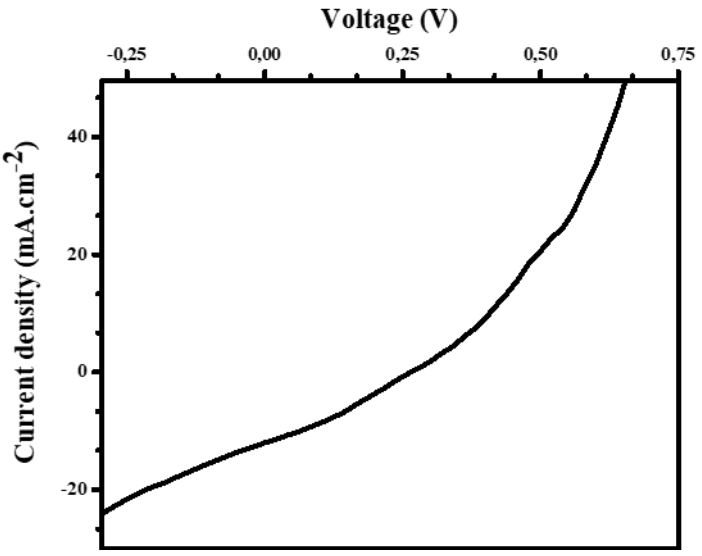

Figure 4-4: J-V curve of the as-prepared $CsPbBr_3$ solar cell.

The XRD data had crystalline phases which may also act as trapping sites. A portion of the photogenerated electrons and holes combine again inside the photovoltaic cell, supplying the internal diode current rather than being injected into the external load, which is how photovoltaic devices function as non-ideal current generators [23]. When electron-hole pairs exclusively decay radiatively, the optimum scenario is reached with minimal recombination energy losses; in this regime, the recombination resistance is maximized along with the cell voltage.

4.3 $CsPbBr_3$/PEABr thin films

4.3.1 Morphology

Figure 4-5 shows the surface morphology of the pristine ($CsPbBr_3$) with and without phenethylammonium bromide (PEABr) additive. *Figure 4-5 (a)* is the pristine thin film that is used to determine the effects of PEABr on the surface of the pristine film, as determined by FEG-SEM microscopy. The pristine thin film appears to have a number of pinholes since the film morphology is driven largely by the surface properties of the substrate [13].

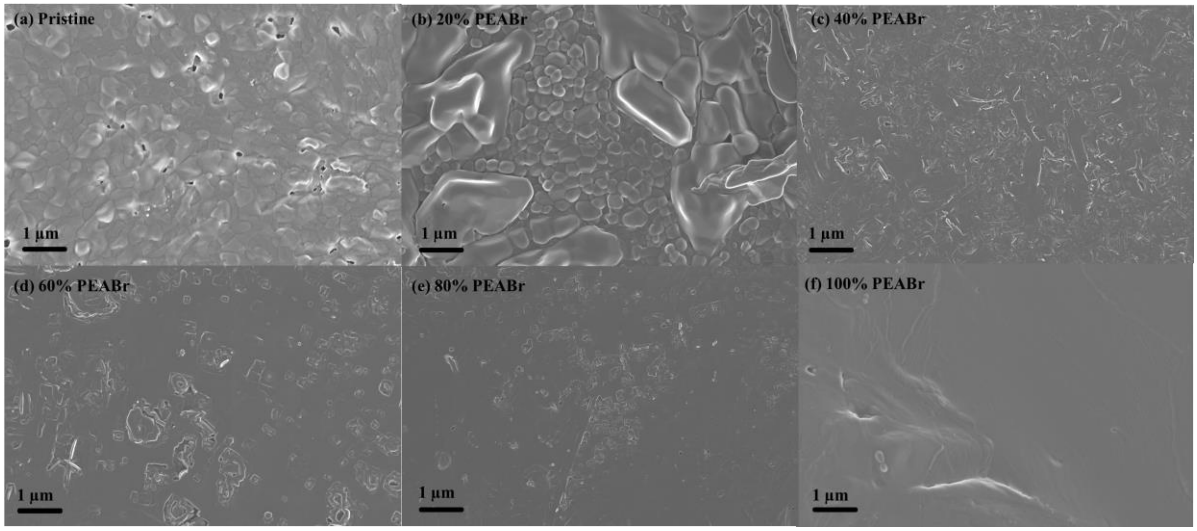

Figure 4-5: SEM micrographs of $CsPbBr_3$ without PEABr and with different mass percent of PEABr.

However, the addition of the long-chain PEABr (*Figure 4-5 (b),(c)(d)(f)*) facilitates the reduction of a pinholes and the formation of large grains as observed in the morphology of the films. The long-chain ammonium with long steric hindrance prevents ions (Cs^+, Pb^{2+}) from continuously entering the forming perovskite crystals and inhibits crystal growth, resulting in smaller particle sizes of the perovskite films [14]. *Figure 4-5(b)* shows what occurs when a layer of 20% PEABr is added on top of a thin film. The average grain size is reduced from 433 nm (pristine) to 209 nm. This phenomenon has been observed in previous reports when a long-chain ammonium is added to a control HaP thin film [15, 16]. Therefore, the reduction of grain size can be attributed to the PEABr additive. The addition of more than 20% PEABr mass percent results in the gradual coverage of the $CsPbBr_3$ thin films as observed from *Figure 4-5(c), (d), (e),* until the pristine thin film is fully covered (*Figure 4-5(f)*).

4.3.2 Optical properties

Figure 4-6 shows the UV-vis absorption spectra of the perovskite film with and without the PEABr additive. According to the absorption spectra, they do not exhibit any characteristic red or blue shift. However, when the PEABr's mass percentage is equal to or greater than 20%, two additional excitonic absorption peaks appear in the short wavelength region. According to previous reports, these phenomena are caused by the formation of quasi-2D perovskites with the formula $PEA_2Cs_{n-1}Pb_nBr_{3n+1}$, where n is the number of inorganic sheets of $[PbBr_6]^{4-}$ between two organic PEA insulating layers [17, 18]. As a result, the two excitonic absorption peaks located at 405 nm and 436 nm have been assigned to the n = 1 and n = 2 phases of the quasi-2D perovskite [15]. As the mass percent of PEABr increases, the

quasi-2D absorption becomes more dominant. These results suggest that the $CsPbBr_3$+PEABr perovskites are composed of mixed-dimensional perovskite phases that contain a variety of quasi-2D structures with varying excitonic energies.

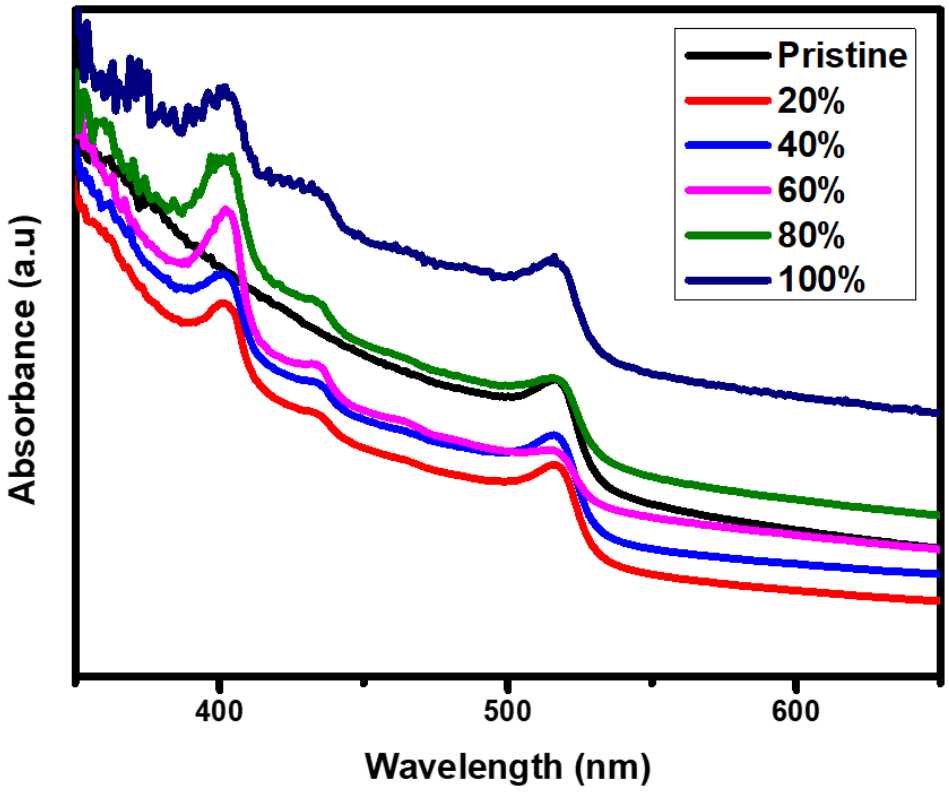

Figure 4-6: Absorbance of $CsPbBr_3$ thin film with and without PEABr.

From the absorbance spectra, the absorbance of the film decreases when 20% PEABr is spin-coated on the pristine film and increases as the mass percentage increases. This phenomenon is likely due to the viscosity of PEABr-isopropanol solution. Thus, the viscosity of the PEABr-isopropanol solution increases with an increase in the mass percent of PEABr in the isopropanol solution. This suggests that at 20% PEABr, the solution is less viscous and during the spin-coating process this solution washes away some amount of the $CsPbBr_3$ film. As a result, a thin layer of the absorbent layer is produced, so the film's absorbance is reduced. As the PEABr mass increases, the solution becomes more viscous, so the pristine film maintains its thickness. When the pristine film is annealed, a 2D layer forms on top of it, and this can facilitate an increase in absorbance with increased PEABr mass percent.

4.3.3 Structural properties

The effects of the PEABr additive on the structural properties of $CsPbBr_3$ thin film were studied using the XRD technique and are shown in *Figure 4-7*. The $CsPbBr_3$ perovskite film is dominated by a cubic (*Pm-3m*) crystal structure. The characteristic peaks at 15.38°, 21.78°, 26.59°, 30.81°, 33.71°, and 37.87° are assigned to the (100), (110), (111), (200), (210), and (211) crystal planes, respectively [6]. With increasing PEABr concentration, the crystal (k00) diffractions become preferentially orientated normally to the substrate, as seen from 10-40θ on the XRD scale.

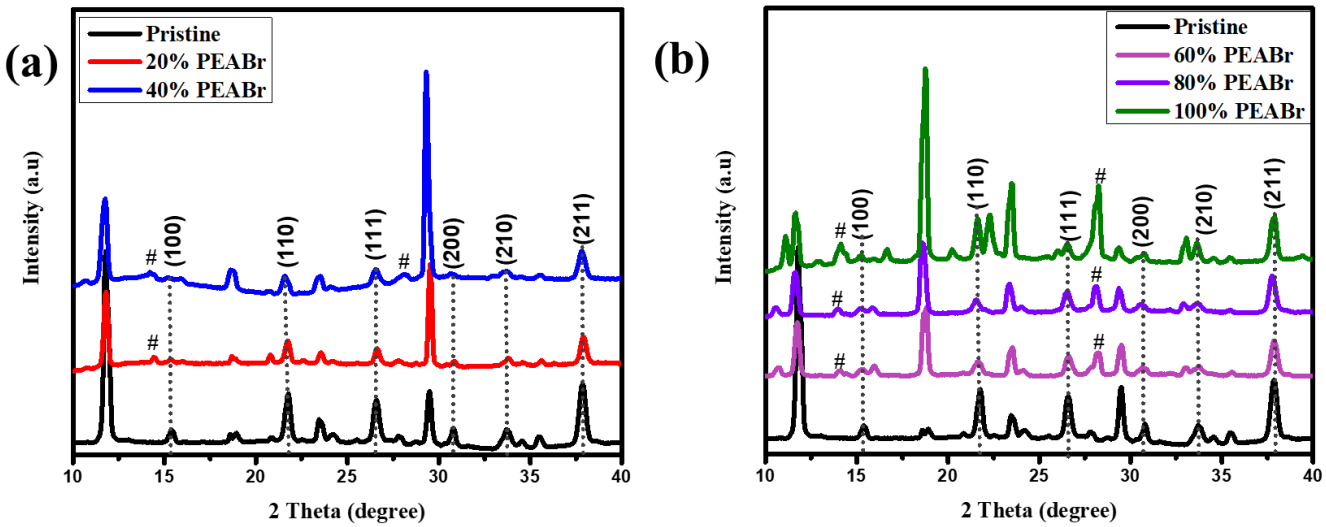

Figure 4-7: XRD patterns of PEABr on FTO/$CsPbBr_3$ thin film from (a) 0% to 40% PEABr (b) 60% to 100% PEABr.

Further, the $CsPbBr_3$ perovskite thin film exhibits the same XRD patterns regardless of the amount of PEABr content in the film. This suggests that the addition of PEABr does not necessarily alter the intrinsic crystal structure of $CsPbBr_3$ perovskite film [18, 19]. PEABr has XRD peaks labeled (#) at 10.58°, 14.13°, 28.14°, and 33.07° in agreement with previous literature [15]. The PEABr diffraction peaks are more obvious when the PEABr mass percent is greater than 40%. Compared to 40% PEABr films, 60 % PEABr films exhibit some roughness, indicating probable PEABr aggregation, which is also supported by UV-vis measurements. PEABr inhibits perovskite crystal formation, resulting in an enhanced film shape and smaller crystallites as shown in table 1.

Table 4-1: FWHM and crystallite size from the 211 peak.

Sample	0% PEABr	20% PEABr	40% PEABr	60% PEABr	80% PEABr	100% PEABr
FWHM	0.3168	0.2094	0.2395	0.2636	0.3062	0.3162
Crystallite size (nm)	25.07	37.92	33.15	30.12	25.94	25.11

As PEABr content increases, the FWHM of the XRD peaks becomes wider. A similar trend is observed in previous reports [15]. However, in this work, the trend is observed when the mass percent is mo 20%, which is consistent with the absorbance results (*Figure 4-6*). From the Scherrer equation, a reduction in the crystallite size derived from the (211) peaks is reduced from 37.92 nm (20% PEABr) to 25.11 nm (100% PEABr), which is consistent with the SEM results [15].

4.4 Performance and photoluminicence $CsMAFAPb(IBr)_3$ solar cells

4.4.1 Photoluminicence (PL) of $CsMAFAPb(IBr)_3$

Figure 4-8 shows the PL of $CsMAFAPb(IBr)_3$ solar cell from the time-resolved photoluminescence spectrometer. The $CsMAFAPb(IBr)_3$ solar cell has a characteristic emission wavelength at 766 nm, which is similar to that of $MAPbI_3$ [15]. A low-intensity peak of the $CsMAFAPb(IBr)_3$ solar cell suggests low levels of recombination that are better in comparison to conventional single cation ABX_3 perovskite solar cells [20]. The bandgap is related to the wavelength by the photon equation:

$$E_g = \frac{1240}{\lambda} eV \qquad \textit{Equation 6}$$

where E_g is the energy gap of the material in eV and λ is the emission wavelength in nm. According to the Shockley-Queisser limit, the maximum efficiency at zero kelvin is found to be 44% for an energy gap of 1.1 eV to 1.4 eV and a wavelength of 1127 nm to 885 nm [21]. The $CsMAFAPb(IBr)_3$ records a high energy bandgap of 1.6 which suggests further improvement for this material.

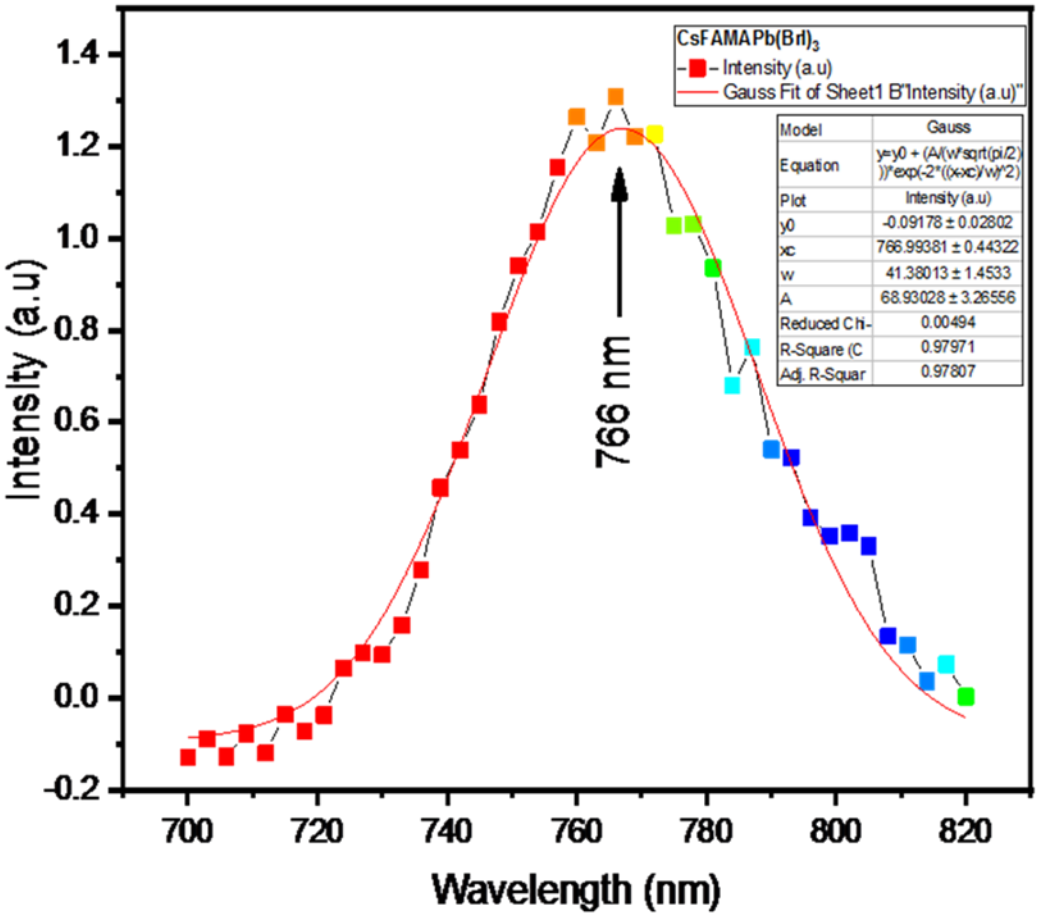

Figure 4-8: Photoluminescence of $CsMAFAPb(IBr)_3$.

4.4.2 Time-Resolved Photoluminescence (TRPL)

The addition of Cs in the MA/FA mixture is responsible for suppressing the yellow phase impurity resulting from the PbI_2 and inducing highly uniform perovskite grains which extend from the hole collecting layer and thus improve the stability of the device. Such devices are currently one of the best-performing perovskite solar cell devices to date [22]. The TRPL of the $CsMAFAPb(IBr)_3$ solar cell is shown in *Figure 4-9*. The TRPL decay is well represented by a bi-exponential decay function that includes a fast component that is related to non-radiative recombination activities (due to the presence of

defects or energy transfer processes) and a gradual decay component associated with radiative recombination [17, 23]. The sample has an estimated lifespan of 24 ns, which implies that the $CsMAFAPb(IBr)_3$ film is less defective. The TRPL decay was determined at a specific emission wavelength that corresponded to the steady-state PL emission peak (*Figure 4-9*).

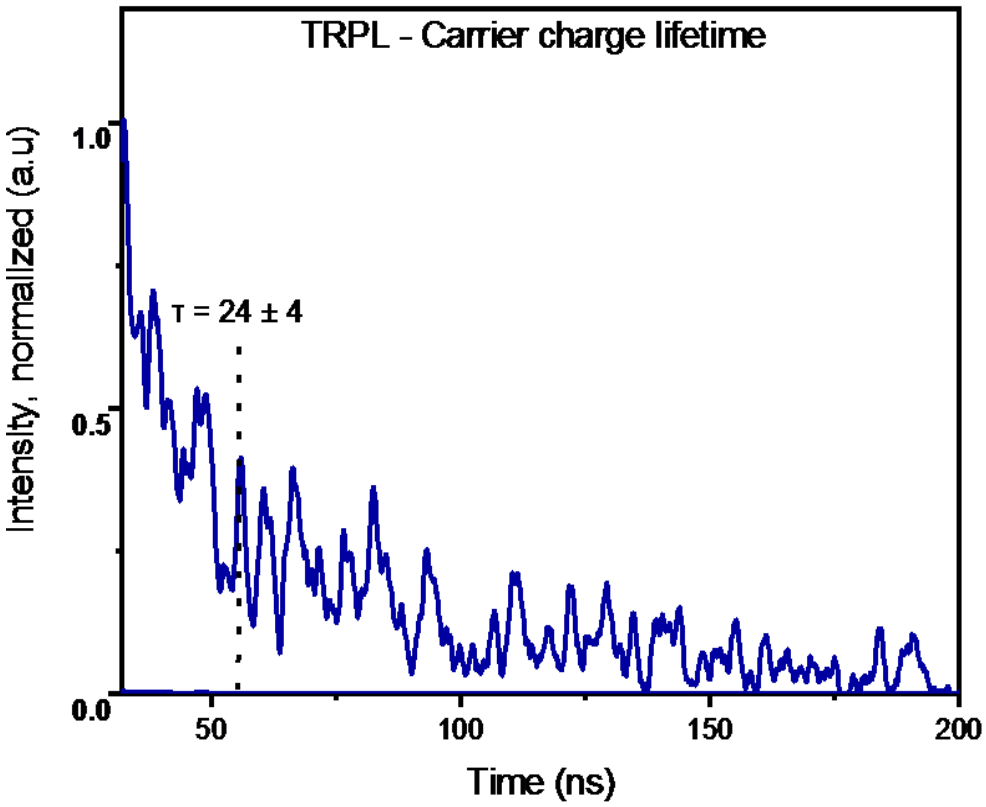

Figure 4-9: TRPL of $CsMAFAPb(IBr)_3$ solar cell.

The measured lifetimes are highly influenced by the emission wavelength, which is in line with the sample's 3D domain [24]. Across the emission wavelength, the lifetime increases by nearly one order of magnitude, from hundreds of ps to a few ns, following the presence of distinct structures.

4.4.3 Solar cell device

Before the beginning of the measurement, no device preconditioning was used, such as mild soaking or a long forward voltage bias. This is similar to the quasi-steady-state conditions proposed by Unger et al. and Kamat [25, 26]. Even during crystallization, a CsMAFA triple cation perovskite reduces

yellow phase impurities, resulting in better film performance regardless of annealing [18]. This enabled a PCE of 13.89% with a V_{oc} of 1.14 eV as well as a Jsc of 23 mA/cm^2. A FF of 57.32% is attained from the I-V graph as shown in *Figure 4-10*. Minimal hysteresis is observed for the CsMAFAPb(IBr)$_3$ solar cell which could be a result of the low voltage scan rate (10 mV/s) as compared to conventional $MAPbI_3$ solar cells [20].

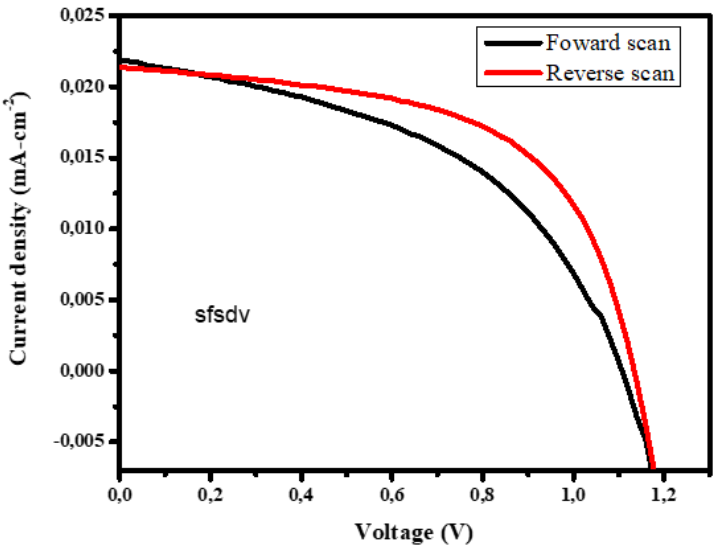

Figure 4-10: I-V measurements of CsMAFAPb(IBr)$_3$.

Before testing, the devices were placed in dark and dry air overnight (below 1 % relative humidity). Roose et al. found that the device efficiency can improve from just a few hours to several days of resting in the dark and dry air. They also noticed that devices may perform poorly and shunting may occur due to preparation errors, contamination caused by chemical/solvent contamination, or degradation of devices [27].

4.5 REFERENCES

1. Yang, X., et al., *Improved photoelectric performance of all-inorganic perovskite through different additives for green light-emitting diodes.* RSC advances, 2019. **9**(59): p. 34506-34511.
2. Li, Y., et al., *High-performance perovskite photodetectors based on solution-processed all-inorganic CsPbBr 3 thin films.* Journal of Materials Chemistry C, 2017. **5**(33): p. 8355-8360.
3. Zhang, Y., et al., *Enhancing the grain size of organic halide perovskites by sulfonate-carbon nanotube incorporation in high performance perovskite solar cells.* Chemical Communications, 2016. **52**(33): p. 5674-5677.
4. Wu, Y., et al., *Retarding the crystallization of PbI 2 for highly reproducible planar-structured perovskite solar cells via sequential deposition.* Energy & Environmental Science, 2014. **7**(9): p. 2934-2938.
5. Nasi, L., et al., *All-inorganic CsPbBr3 perovskite films prepared by single source thermal ablation.* Frontiers in chemistry, 2020. **8**: p. 313.
6. Liu, D., et al., *Two-step method for preparing all-inorganic CsPbBr3 perovskite film and its photoelectric detection application.* Materials letters, 2017. **186**: p. 243-246.
7. Feng, J., et al., *Curing the fundamental issue of impurity phases in two-step solution-processed CsPbBr3 perovskite films.* Science Bulletin, 2020. **65**(9): p. 726-737.
8. Muhammed Shafi, P. and A. Chandra Bose, *Impact of crystalline defects and size on X-ray line broadening: A phenomenological approach for tetragonal SnO2 nanocrystals.* AIP Advances, 2015. **5**(5): p. 057137.
9. Liang, Z., et al., *A large grain size perovskite thin film with a dense structure for planar heterojunction solar cells via spray deposition under ambient conditions.* RSC advances, 2015. **5**(74): p. 60562-60569.
10. Jeon, N.J., et al., *Solvent engineering for high-performance inorganic–organic hybrid perovskite solar cells.* Nature materials, 2014. **13**(9): p. 897-903.
11. de Quilettes, D.W., et al., *Impact of microstructure on local carrier lifetime in perovskite solar cells.* Science, 2015. **348**(6235): p. 683-686.
12. Gedamu, D., et al., *Solvent-antisolvent ambient processed large grain size perovskite thin films for high-performance solar cells.* Scientific reports, 2018. **8**(1): p. 1-11.
13. Li, C., et al., *Highly compact CsPbBr3 perovskite thin films decorated by ZnO nanoparticles for enhanced random lasing.* Nano Energy, 2017. **40**: p. 195-202.
14. Wang, D., et al., *Amplified spontaneous emission properties of solution processed CsPbBr 3 perovskite thin films doped with large-group ammonium cations.* Optical Materials Express, 2020. **10**(4): p. 981-997.
15. Ban, M., et al., *Solution-processed perovskite light emitting diodes with efficiency exceeding 15% through additive-controlled nanostructure tailoring.* Nature communications, 2018. **9**(1): p. 1-10.
16. Liu, Y., L.K. Ono, and Y. Qi, *Organic additive engineering toward efficient perovskite light-emitting diodes.* InfoMat, 2020. **2**(6): p. 1095-1108.
17. Byun, J., et al., *Efficient visible quasi-2D perovskite light-emitting diodes.* Advanced Materials, 2016. **28**(34): p. 7515-7520.

18. Ng, Y.F., et al., *Highly efficient Cs-based perovskite light-emitting diodes enabled by energy funnelling.* Chemical Communications, 2017. **53**(88): p. 12004-12007.
19. Ling, Y., et al., *Enhanced optical and electrical properties of polymer-assisted all-inorganic perovskites for light-emitting diodes.* Advanced Materials, 2016. **28**(40): p. 8983-8989.
20. Sum, T.C., et al., *Energetics and dynamics in organic–inorganic halide perovskite photovoltaics and light emitters.* Nanotechnology, 2015. **26**(34): p. 342001.
21. Sachenko, A., et al., *Temperature dependence of photoconversion efficiency in silicon heterojunction solar cells: Theory vs experiment.* Journal of Applied Physics, 2016. **119**(22): p. 225702.
22. Saliba, M., et al., *Cesium-containing triple cation perovskite solar cells: improved stability, reproducibility and high efficiency.* Energy & environmental science, 2016. **9**(6): p. 1989-1997.
23. Liang, P.W., et al., *Additive enhanced crystallization of solution-processed perovskite for highly efficient planar-heterojunction solar cells.* Advanced materials, 2014. **26**(22): p. 3748-3754.
24. Yuan, M., et al., *Perovskite energy funnels for efficient light-emitting diodes.* Nature nanotechnology, 2016. **11**(10): p. 872-877.
25. Christians, J.A., J.S. Manser, and P.V. Kamat, *Best practices in perovskite solar cell efficiency measurements. Avoiding the error of making bad cells look good*. 2015, ACS Publications. p. 852-857.
26. Unger, E.L., et al., *Hysteresis and transient behavior in current–voltage measurements of hybrid-perovskite absorber solar cells.* Energy & Environmental Science, 2014. **7**(11): p. 3690-3698.
27. Roose, B., et al., *Spontaneous crystal coalescence enables highly efficient perovskite solar cells.* Nano Energy, 2017. **39**: p. 24-29.

5 Conclusion and future work

5.1 Conclusion

This study was focused on investigating the morphological, optical, and structural properties of cesium lead tribromide ($CsPbBr_3$) using scanning electron microscopy (SEM), ultraviolet-visible spectroscopy (UV-Vis), and X-ray diffractometer (XRD), respectively. Furthermore, the influence of phenethylammonium bromide (PEABr) on the $CsPbBr_3$ thin film was also investigated using these characterization techniques. The current density-voltage (J-V) properties of $CsPbBr_3$ and $CsMAFAPb(IBr)_3$ solar cells with the architecture ($FTO/TiO_2/CsPbBr_3$/Spiro-MeOTAD/silver) and ($FTO/TiO_2/CsMAFAPb(IBr_3)$/Spiro-MeOTAD/gold), respectively were measured. The photoluminescence (PL) and lifetime of the charge carrier for $CsMAFAPb(IBr_3)$ solar cell were also studied using time-resolved photoluminescence (TRPL).

In section 4.2, a thin film of $CsPbBr_3$ was synthesized using the classical two-step solution method. The SEM micrographs of this thin film show a discontinuous morphology with pinholes caused by poor surface coverage. The large grain size of the material, 433 nm, can also be an advantage in solar cell applications due to the higher carrier mobilities associated with large grain size halide perovskites (HaP). Optical studies of $CsPbBr_3$ revealed an absorbance onset and excitonic peaks at 530 and 515 nm, respectively. XRD results revealed a cubic (P*m*-3*m*) crystal structure with the lattice parameters of $a = b = c = 5.830$ Å. The two-step solution methods for preparing $CsPbBr_3$ thin are accompanied by impurity phases of $CsPb_2Br_5$, shown by XRD patterns. The impurity phases in $CsPbBr_3$ thin film are caused by the conversion medium (methanol). Therefore, using a different conversion medium such as 2-methoxyethanol, among others, to finely control the reaction between CsBr and $PbBr_2$ which will yield a single-phase $CsPbBr_3$ thin film is recommended. J-V measurements were performed on the $CsPbBr_3$ solar cell to study the characteristics such as the fill factor (FF), short circuit current (J_{sc}), open-circuit voltage (V_{oc}), and power conversion efficiency (PCE). The solar cell had a low FF and J_{sc} of 30.89% and 12.02 mA/cm^{-2} due to pinholes in the $CsPbBr_3$ thin film. The device produced a low V_{oc}, 0.3 eV, and a low PCE, 0.94 %, due to shunting caused by the direct contact between the ETL and HTL pinholes.

In section 4.3 we demonstrated the growth of $CsPbBr_3$/PEABr by spin-coating a solution of PEABr-isopropanol on the as-prepared $CsPbBr_3$ thin film on the FTO substrate. The PEABr-isopropanol solutions contained different mass percentages of phenethylammonium bromide (PEABr). SEM micrographs showed that the PEABr induced full surface coverage, and reduced the grain size of $CsPbBr_3$

thin film at 20% PEABr, as well as a reduced pinholes on the surface of the films. Furthermore, when more than 20% PEABr is added to the $CsPbBr_3$ thin film, a layer forms on top of the as-prepared $CsPbBr_3$ film. The optical study of $CsPbBr_3$/PEABr showed two additional excitonic peaks at 405 and 436 nm. These peaks were attributed the formation of n = 1 and n = 2 phase of a quasi-2D $PEA_2Cs_{n-1}Pb_nBr_{3n+1}$ perovskite. The viscosity of the PEABr-isopropanol solution played a role in the absorbance of the thin film. The less viscous (20% PEABr) solution was responsible for removing a certain amount of the $CsPbBr_3$ film which resulted in a reduced absorbance of the film. The absorbance increased as the viscosity increased and thus increasing the excitonic peak of the quasi-2D perovskite. The structural properties revealed that the mass percent of PEABr does not necessarily affect the crystal structure of $CsPbBr_3$ perovskite. However, a few PEABr peaks appeared on the XRD result as the crystallinity of the film increased. The fullwidth at half maximum (FWHM) decreased from 0.3168 to 0.2094 when 20% PEABr is spin-coated on the as-prepared $CsPbBr_3$ and began to increase when more than 20% PEABr is spin-coated in the film. This was found to be consistent with the optical properties of the films.

In section 4.4 we discussed the synthesis of a $CsMAFAPb(IBr)_3$ solar cell device, including its characterization using the TRPL spectroscopy and J-V measurements. The TRPL spectroscopy also enabled us to determine the photoluminescence (PL) of the $CsMAFAPb(IBr)_3$ material. The PL of the $CsMAFAPb(IBr)_3$ material revealed an emission wavelength of 766 nm which was used to determine the energy bandgap of 1.6 eV. We concluded that, according to the Shockley-Queisser limit, this material suggested further improvement because it has not reached its limit. The TRPL also revealed that the $CsMAFAPb(IBr)_3$ sample has an estimated lifetime of 24 ns. From these results, we deduced that this material is less defective. This is supported by the J-V measurements which revealed that the $CsMAFAPb(IBr)_3$ solar cell device has a high PCE of 13.89% and a V_{oc} of 1.14 eV. A J_{sc} of 23 mA/cm^2 was produced by the device and a reasonable FF of 57.32 %. We recommend that the synthesis and characterizations of HaP solar cells should be done in a nitrogen-filled glovebox because HaP suffers from fast degradation due to moisture and the presence of oxygen.

5.2 Future work

In the future, we will fabricate a solar cell device of $CsPbBr_3$/PEABr to find the necessary mass percent of PEABr require for solar application by comparing J-V measurements. We also plan to synthesize and characterize the $CsMAFAPb(IBr)_3$ thin film to clearly understand the film characteristics.